THESIS

DEVELOPMENT OF PLASMA CLEANING AND PLASMA ENHANCED CLOSE SPACE SUBLIMATION HARDWARE FOR IMPROVING CdS/CdTe SOLAR CELLS

Submitted by

Drew Swanson

Department of Mechanical Engineering

In partial fulfillment of the requirements

For the Degree of Master of Science

Colorado State University

Fort Collins, Colorado

Fall 2012

Master's Committee:

Advisor: John Williams
Co-Advisor: W.S. Sampath

James Sites

ABSTRACT

DEVELOPMENT OF PLASMA CLEANING AND PLASMA ENHANCED CLOSE SPACE SUBLIMATION HARDWARE FOR IMPROVING CdS/CdTe SOLAR CELLS

A scalable photovoltaic manufacturing process that employs a heated pocket deposition technique has been developed at Colorado State University. It allows for the economical manufacturing of single-junction thin-film CdTe solar cells with efficiencies over 13%. New techniques that further increase cell efficiency and reduce production expenses are required to make solar energy more affordable. To address this need a hollow-cathode plasma source was added to the load-lock region of the CSU single-vacuum in-line CdTe-cell fabrication system. This plasma source is used to clean the transparent-conductive-oxide layer of the cell prior to the deposition of the CdS and CdTe layers. Plasma cleaning enables a reduction in CdS thickness by approximately 20 nm, while maintaining an improved cell voltage. Cell current was improved and cell efficiency was increased by 1.5%. Maps generated by scanning white-light interferometry, electroluminescence, and light-beam-induced current all show uniformity improvement with plasma cleaning treatment. To further increase cell efficiency a hollow-cathode plasma-enhanced close space sublimation (PECSS) source was utilized to modify the CdS window layer material as it was being deposited. This was done by integrating PECSS into the CSU inline CdS/CdTe-cell fabricating system and by sublimating the CdS semiconductor material through a plasma discharge. To date oxygenated CdS (CdS:O) cells have been grown by sublimating CdS through a PECSS source operated on oxygen. Data are presented showing that

PECSS CdS:O films have increased the band gap of the window layer therefore reducing absorption loss, increasing cell current, and improving efficiency by 1.2%.

ACKNOWLEDGEMENTS

I would like to thank first and foremost my advisor, Dr. John Williams for his guidance and extensive support throughout the Master's degree program. Additionally, I would like to thank my co-advisor W.S. Sampath and committee member Dr. James Sites for their conversation, knowledge, and guidance through this research. A big thank you goes to Abound Solar, specifically Richard Hafer, Jeff Wicks, and Keegan Barricklow for their collaborative research in scaling the plasma cleaning technology. I would like to thank the following gentleman for their help and training on these various characterization techniques: Jack Clark with Scanning White Light Interferometry, Dr. Pat McCurdy with XPS, EDS, and SEM imaging, and Don Heyse with AFM and UV-Vis. A special thanks to the graduate students in the Physics PV Characterization lab, specifically Russell Geisthardt, Tyler McGoffin, John Raguse, for their help in device characterization (J-V, JVT, QE, EL, and LBIC). I would like to thank associate researchers Jennifer Drayton, Kevan Cameron, and Kurt Barth, fellow graduate researchers Garrett Metz, Pavel Kobyakov, and Jason Kephart, and undergraduate researchers Ryan Lutze, and Sam Hafner for all of their contributions to this work. A large heartfelt thank you to my mom and dad, Shelli and Ken Swanson, my brother Bryan and the rest of my extended family, if it wasn't not for you I would not have made it this far in my academic career. Lastly I would like to thank my girlfriend Lauren Bowers (B), and dogs Sinatra and Monroe for their never ending love and companionship. Work for this thesis was supported originally by the NSF I/UCRC at Colorado State, more recently by the DOE F-PACE program and in part by a NTU scholarship.

TABLE OF CONTENTS

LIST OF TABLES

LIST OF FIGURES

Chapter I Introduction

The world consumed an amount of energy equivalent to 13 billion tonnes of oil last year [1], which is equal to less than the amount of solar radiation that falls onto the earth's surface in one day. Photovoltaic cells are one technique for converting solar radiation to electrical power. This thesis will focus on the improvements to photovoltaic (solar) cell efficiency through the use of plasma processing in advanced CdTe solar cell manufacturing. Chapter I will outline the demand for alternative energy, provide justification for continued research in PV, and present an overview of photovoltaic physics. The material and device characterization techniques used for understanding the results obtained with plasma-aided solar cell manufacturing are outlined in Chapter II. The primary results of this research are described in Chapter III, which demonstrate a plasma cleaning treatment of transparent conductive tin oxides, which allows a thinner CdS film to be used and higher efficiency devices to be fabricated. Chapter IV will describe the integration of a plasma discharge into a close space sublimation source that allowed the incorporation of oxygen into CdS films for improved transparency. Chapter V contains conclusions from Chapters III & IV and an outline of future work on plasma-aided solar cell manufacturing techniques.

1.1 Growing Energy Demand

Energy demands are escalating as the world population continues to grow. The population is now over 7 billion with current trends projecting a 20% growth in the next 20 years (Figure 1A). Energy consumption growth follows suit, with a 40% increase in the global energy demand and an 80% increase in global electricity demand by 2030.

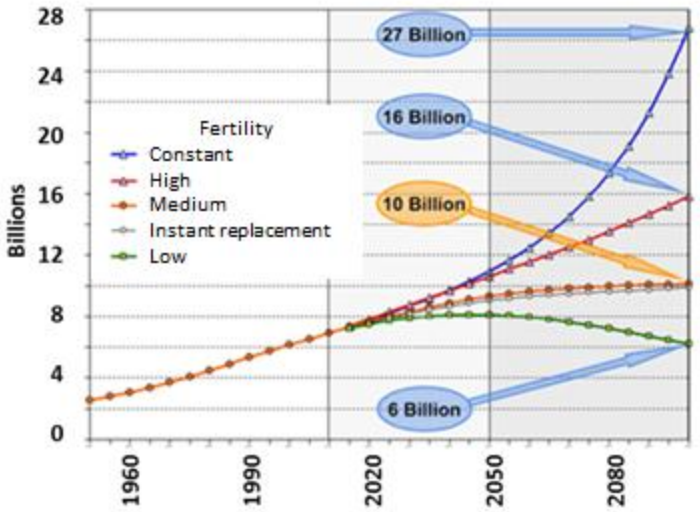

Figure 1A Increasing global population (UN Population Division, 2010) [2].

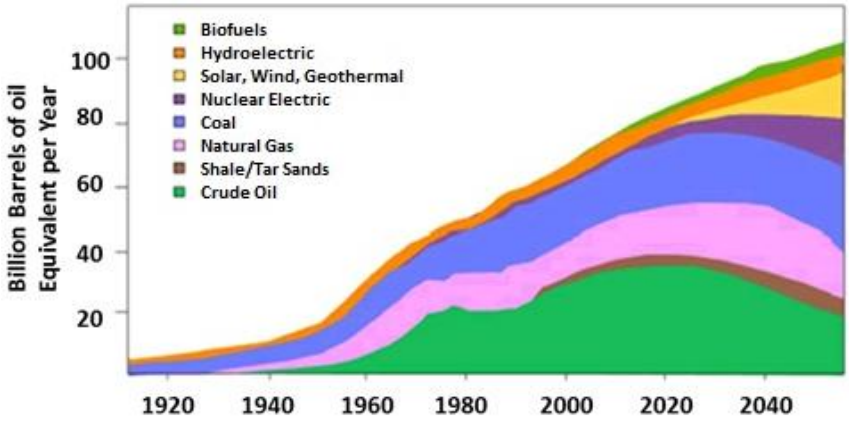

Figure 1B Energy consumption (Orr, 2006) [3].

To subsidize this growing demand multiple sustainable energy supplements are being developed (Figure 1B), not only to level off depletion rates of limited resources such as crude oil, but to also limit the environmental impacts caused from combustion. Since 1950 carbon emissions have increased with energy demand (Figure 2A). Although there is much debate over how much carbon dioxide accumulation is needed to make the earth uninhabitable [4, 5], it is

agreed that CO_2 production is increasing and global temperatures are rising (Figure 2B). Some researchers and policy makers believe that with an investment in a suite of renewable energy sources, we can limit the environmental impact and sustain a technologically advanced standard of living for all countries.

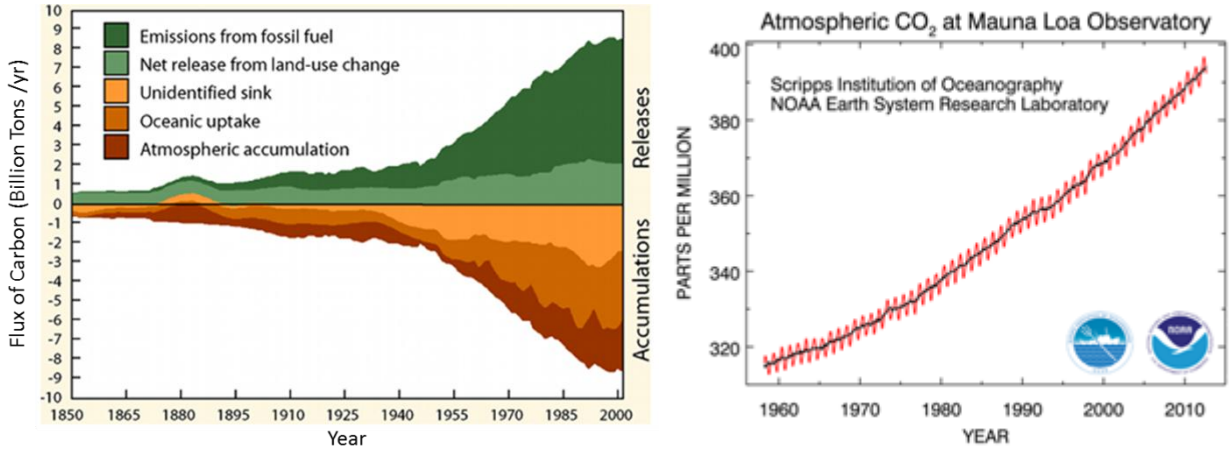

Figure 2 A: Flux of carbon per year (Hoffman, 2008) [6] B: Carbon dioxide concentration timeline (Tans, 2012) [7].

1.2 Renewable Energy

The United States (US) generates less than 4% of its power from renewable energy sources whereas Europe currently generates over 17% (both excluding hydroelectricity) [8,9]. This occurred because Europe has aggressively promoted renewable energy development, taking several technologies to implementation scales that compete with coal and nuclear power. Figure 5 shows the growth of renewable power capacity in Europe from 2000 to 2011. Significant contributions from wind and photovoltaic energy production (PV) were achieved while fuel oil and coal consumption were reduced.

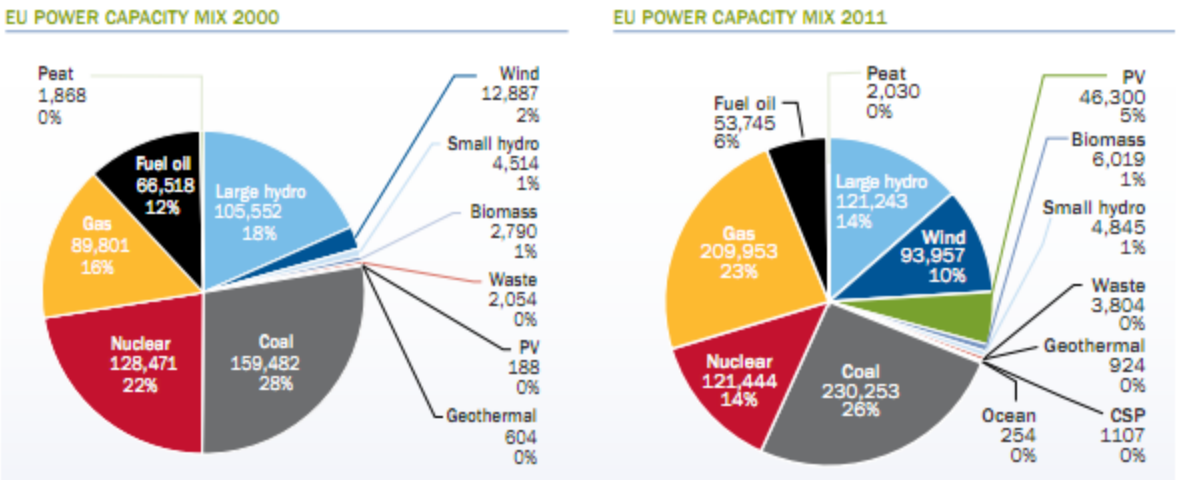

Figure 3 Power capacity by energy source for Europe 2000 (Left) and 2011 (Right) (Zachary, 2010) [9].

The United States has begun to grow its renewable energy capacity, increasing wind capacity by 39% and solar PV capacity by 52% in 2009 (Figure 4) [8]. Geothermal and hydro power generation have remained relatively constant since 2000, as the United States is predominantly growing in wind and PV technologies. With strong potential as the radiation from the sun supplies the earth with tremendous amounts of energy every day. The amount of solar energy reaching the surface of the planet is so vast that in one year it is about twice as much as will ever be obtained from all of the Earth's non-renewable resources of coal, oil, natural gas, and mined uranium combined [10]. This makes investment in solar a promising area for development into a dominate renewable energy source of the future.

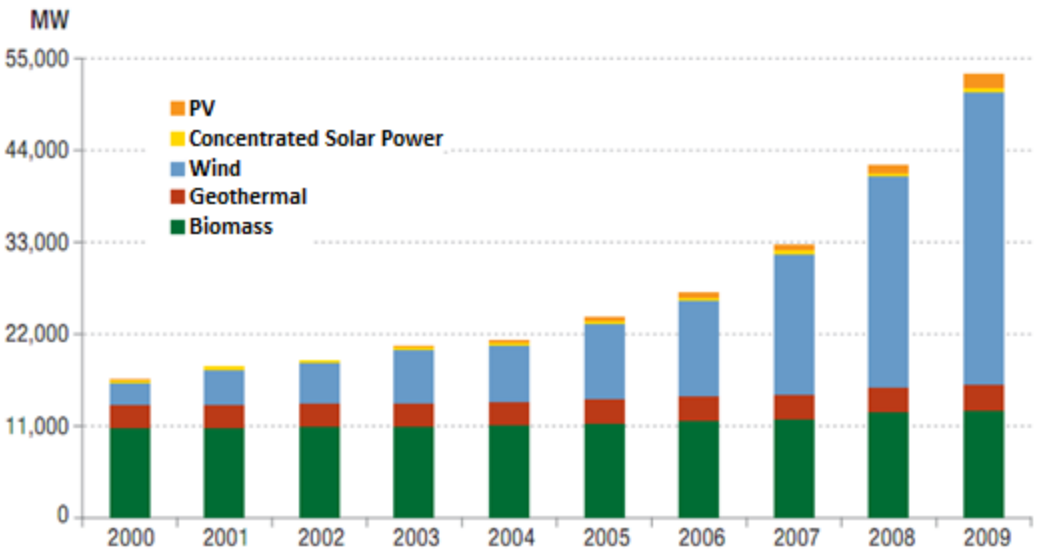

Figure 4 Renewable electricity generation capacity for the United States by source (excluding hydropower) (US DOE, 2010) [8].

To initiate PV growth, the United States Department of Energy has developed research programs such as the SunShot initiative, which aims to develop solar cell technologies that will reduce the cost of solar energy systems by 75% before the end of the decade. Reaching this goal will make solar energy cost-competitive with conventional forms of electricity without subsidies. It is believed this will enable widespread development across the United States [11]. The venture capital and private equity investment in solar technologies has increased from 5 million in 2001 to 1 billion in 2009 making solar energy the renewable technology of choice in the US [8].

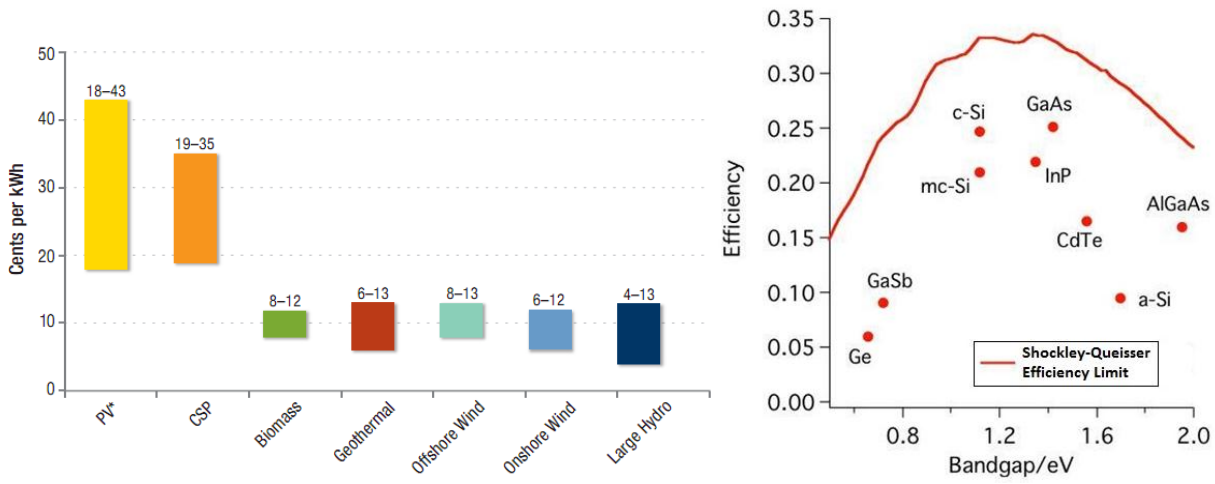

Figure 5 A: United States PV power sales price (US DOE, 2010) [8] B: Current solar cell Efficiency vs. Potential efficiency (Shockley, 1961) [12].

Reductions in the cost of solar power generation (price/watt) over the past decade have supported exponential growth in PV manufacturing; however, there still remains the potential for further reduction in cost (Figure 5A). Although cost will continue to drop through production scaling, the current state of the art PV technologies reveal a large difference between theoretical maximum efficiency limits and cell efficiencies of current devices (Figure 5B). New techniques to increase solar cell efficiency will help to further reduce PV costs.

1.3 PV Fundamentals

Photovoltaic cells convert sun light directly to electricity through the use of semiconductor materials. To understand this process consider basic band theory where the electrons in a material develop distinct bands at various energy levels. These bands are separated by regions with no available states, where the electrons are forbidden to exist. The bands and their relation to each other dictate material properties such as electrical resistivity,

transparency to light, electroluminescence, and photoelectric effect. The two bands of interest in PV phenomenon are the bands known as the conduction and valence band.

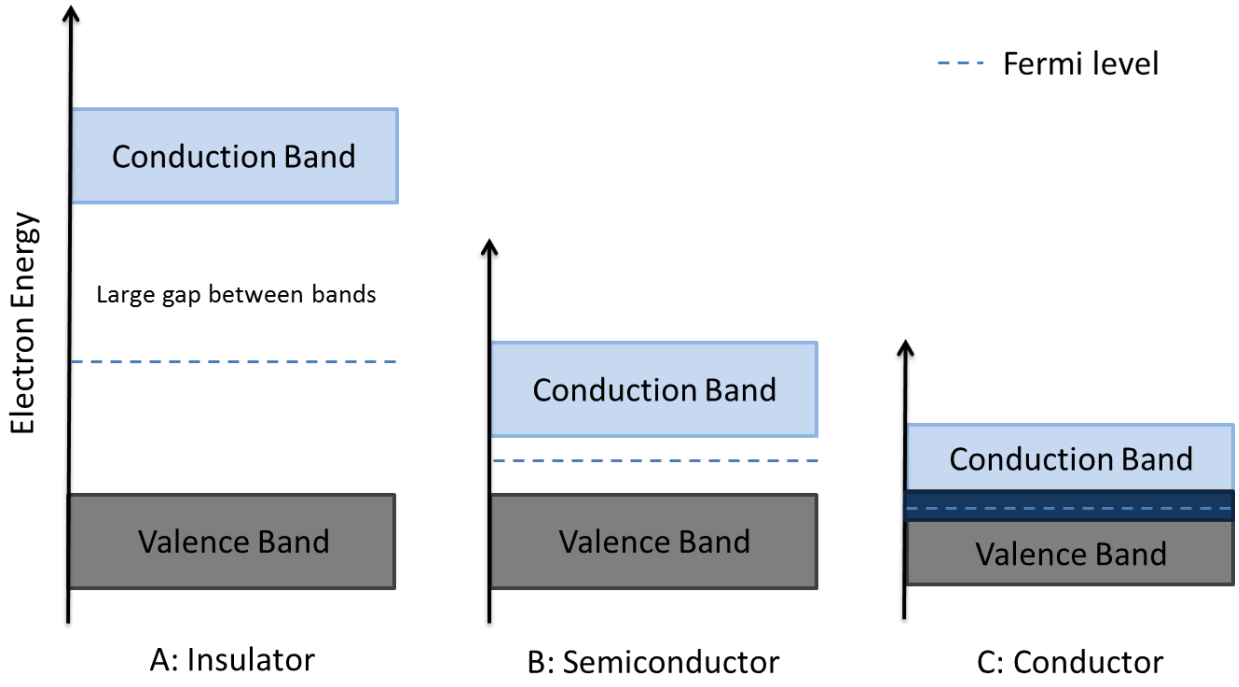

Figure 6 Band theory of conductors, semiconductors, and insulators [13].

The position of these two bands dictates how the material is categorized as suggested in Figure 6 [14]. In a conductor (Figure 6C) the bands overlap allowing an electron to move freely around due to states that are empty within the upper portion of the band. In some materials, a band can be completely filled with electrons making it impossible for them to move around freely. The upper most filled band is called the valance band, and the next band above is referred to as the conduction band. When an electron gets from the valence band to the conduction band it can again move freely. As these bands become separated in a semiconductor and insulator, a significant outside source of energy is required to move an

electron from the filled valence band to the conduction band. This gap between bands is defined as the band gap (E_g) and the magnitude of this gap is the defining characteristic between a semi-conductor and insulator. A semi-conductor is essentially an insulator with a smaller band gap. At zero degrees kelvin the valence band of a semiconductor is completely filled, and the conduction band is completely empty. As the temperature increases a few electrons in the tail of the electron energy distribution will have enough energy to move from the valence band to the conduction band. This action leaves behind holes, the absence of an electron, in the valence band which are also free to move. Both holes in the valence band and electrons in the conduction band are free charge carriers that contribute to the conduction of current in semiconductor materials.

A band gap is characterized as being either direct or indirect. The band gap is representative of the minimum energy required for an electron to move from the valence band to the conduction band, but the top of the valence band and bottom of the conduction band do not always have the same electron momentum. In a direct band gap material the top of the valence band and the bottom of the conduction band are at the same electron momentum, allowing an absorbed photon with energy above the band gap energy to generate a hole-electron pair (Figure 7A). In an indirect band gap the top of the valence band and bottom of the conduction band do not lie at the same electron momentum and so additional energy from lattice vibrations (photons) are needed to generate a hole-electron pair (Figure 7B). As a consequence of the need for electron-phonon interactions, indirect absorbers require substantially more material to absorb the same amount of light compared to a direct band gap material. As an example an indirect material such as silicon will require 100 times more material

to absorb the same amount of light as a direct band gap material such as copper indium gallium selenide (CIGS) or cadmium telluride (CdTe). Furthermore indirect band gap materials require higher quality material for solar cell production to prevent hole-electron recombination before the separated free carriers can be swept out of the material and used to produce PV energy.

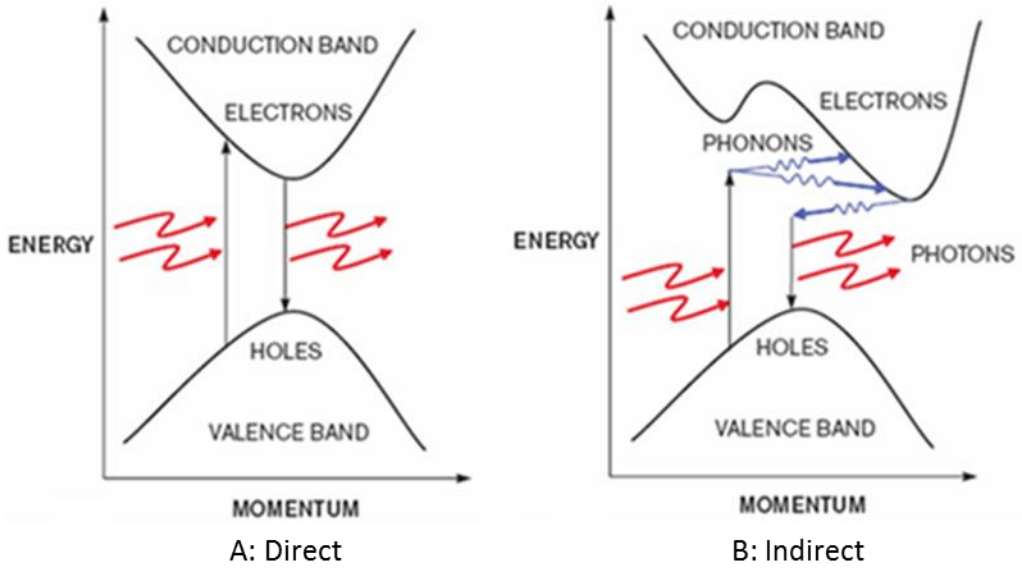

Figure 7 Energy vs. Momentum diagram for A: Direct and B: Indirect band materials (Rako, 2010) [15].

Semiconductors can further be classified as intrinsic and extrinsic. An Intrinsic semiconductor is defined as having no impurities, which can strongly affect the number and type of charge carriers. Intrinsic materials and the number of free holes and free electrons are equal. Intrinsic materials are turned extrinsic by incorporating impurities, known as dopants, into the lattice structure. Extrinsic semiconductors that have been doped to have impurities that are acceptors of electrons are known as positive type (p-type). Semiconductors doped to have impurities that are donors of electrons are known as negative type (n-type). For example,

a common semiconductor like silicon can be doped p-type by adding boron or n-type by adding phosphorus. The Fermi energy level is defined as the energy level with a 50% probability of being occupied. Intrinsic materials have the same number of electrons and holes and so the Fermi level is near the center of the band gap. The position of the Fermi level in extrinsic materials is a function of the concentration of donors and acceptors, their energy level, and the temperature of the material. The Fermi level moves up or down to maintain a charge density balance between the concentrations of free charge carriers and immobile ionized dopants.

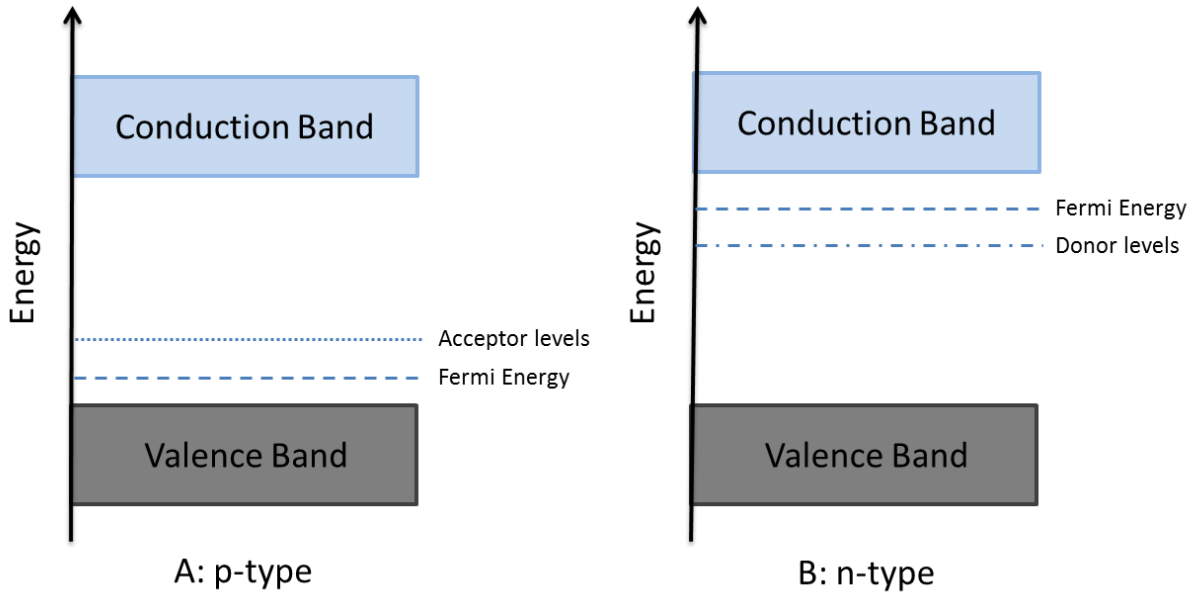

Figure 8 Position of Fermi energy A: p-type and B: n-type semiconductors.

P-type materials have the Fermi level shifted towards the valence band because of the presence of dopants at the acceptor energy state (Figure 8A). N-type materials have the Fermi level shifted toward the conduction band due to presence of dopants at a donor energy state (Figure 8B). As separate materials the Fermi levels do not align (Figure 8A), however when the n-type and p-type materials are brought together a p-n junction is formed, which is referred to

as a diode. At equilibrium and without the presence of photons and temperature gradients, the Fermi levels in the two materials must be the same on each side of the junction causing the bands to bend as shown in Figure 9A. As the bands bend a net negative charge imbalance sets up in the p-type region adjacent to the junction and a net positive charge imbalance sets up in the n-type region. These charge imbalances are caused by donor and acceptor ions in the n-type and p-type regions respectively. The collective volume of these two space charge regions is called the deletion width of the diode. The magnitude of the space charge in each material must be equal. These adjacent positive and negative space charge regions develop an electric field that retard further diffusion of majority charge carriers, this field is referred to as the built-in-field.

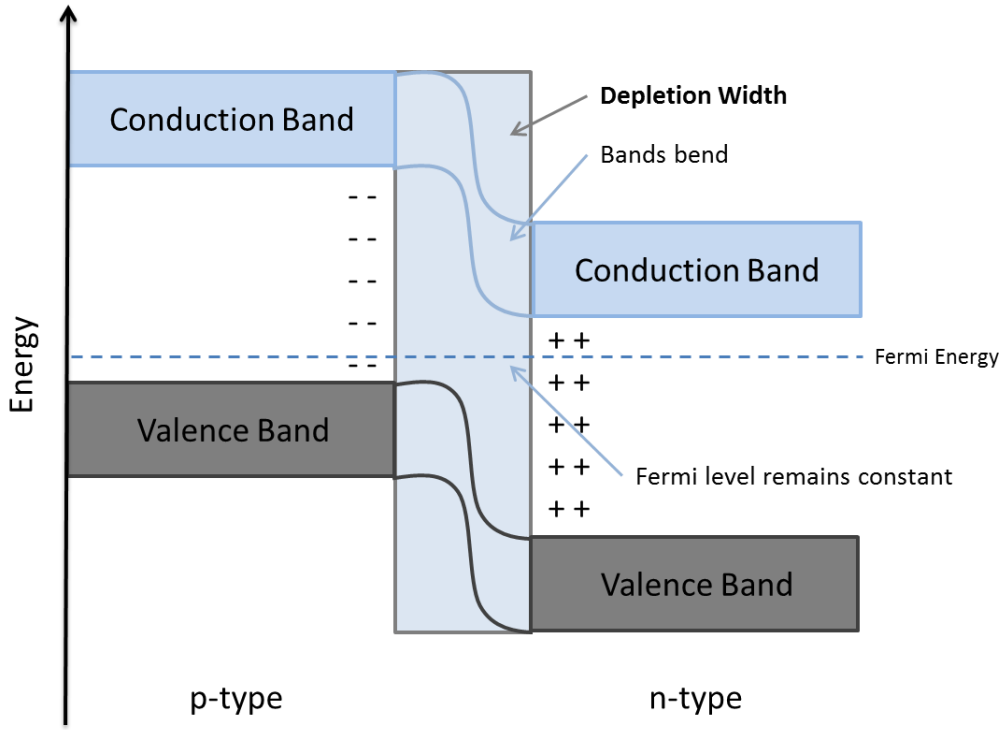

Figure 9A The p–n junction [14].

There are two types of p-n junctions, a hetero-junction or a homo-junction. Homo-junctions use the same semiconductor material, which is doped to form both the p-type and n-type regions. Hetero-junctions are formed using different materials for the n-type and p-type. In general the interface of a homo-junction device is superior since the same base material is used on both sides of the junction. This limits the formation of energy barriers and recombination sites that reduce cell efficiency. Hetero-junctions allow for the window layer and absorber layer band gaps to be engineered around the solar spectrum to limit absorption losses, but they often suffer from losses due to energy barriers and recombination sites.

As a diode is exposed to light, photons are absorbed and hole-electron pairs are generated within the depleted width region. The built-in-field will push the electron towards the n-type and the hole towards the p-type. The Fermi energy and built-in-field will adjust to allow the flow of electrons and holes from the majority charge carriers to balance the photo-generated current. As the electrons and holes build up, the Fermi level will change across the diode establishing a voltage difference between the front and back contacts (Figure 9B). This voltage difference developed under light illumination at an open circuit condition is known as the open circuit voltage (V_{oc}) of the photodiode.

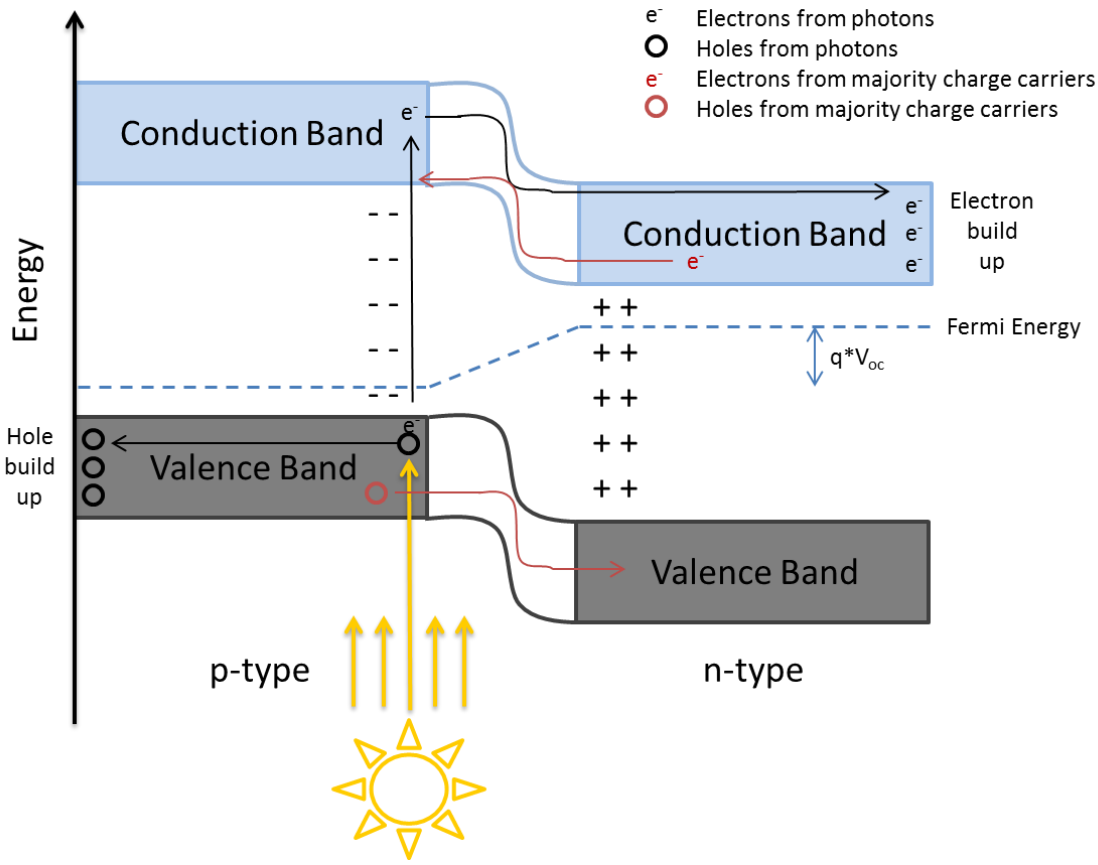

Figure 9B p-n junction under photon bias.

If the photon generated hole-electron pairs are swept out of the diode region and complete the circuit to the back contact under no load, a short circuit current is generated. As a constant flux of photons are absorbed, for example from the AM 1.5 solar spectrum displayed in Figure 10A, a constant flux of electrons will flow through the circuit. The current at this short circuit condition is called the short circuit current, commonly denoted per unit area giving a short circuit current density (J_{sc}) (mA/cm^2).

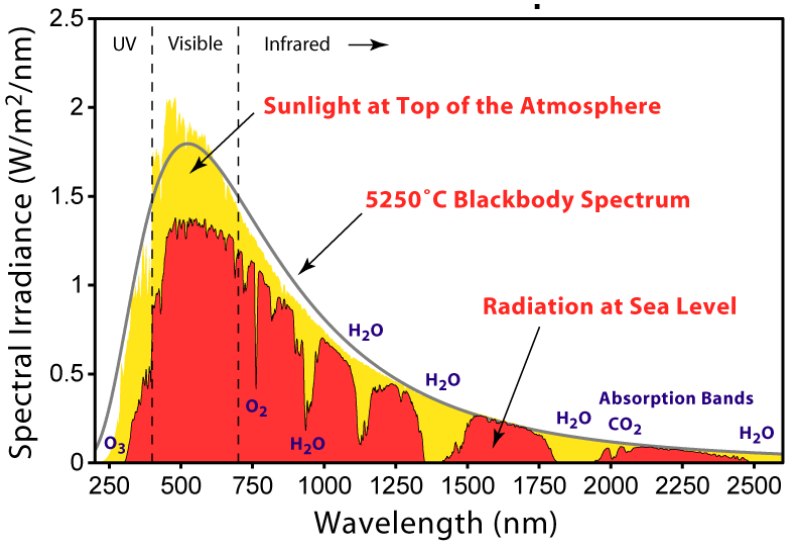

Figure 10A AM 1.5 solar radiation spectrum (NREL, 2012) [16-18].

The V_{oc} and J_{sc} conditions are standard parameters used to describe the performance of a photodiode however neither point will generate power. At the open circuit voltage condition there is no current flow and similarly at the short circuit current condition there is no voltage potential, both result in no power output. As a load resistance is varied between the open circuit and short circuit condition, a current density vs. voltage (J-V) curve is generated (Figure 10B). The parameters J_{sc} and V_{oc} are represented by the axis intercepts of the solid line, the dashed line represents the power generation at any given point along the load sweep. The maximum power point (mp) is represented in Figure 10B corresponding to the maximum power voltage (V_{mp}) and maximum power current density (J_{mp}) of the cell. Fill factor (FF) is a characteristic parameter comparing the max power point to the product of open circuit voltage and short circuit current (Equation 1.1). The higher the FF the closer the max power point will be to the potential max power point.

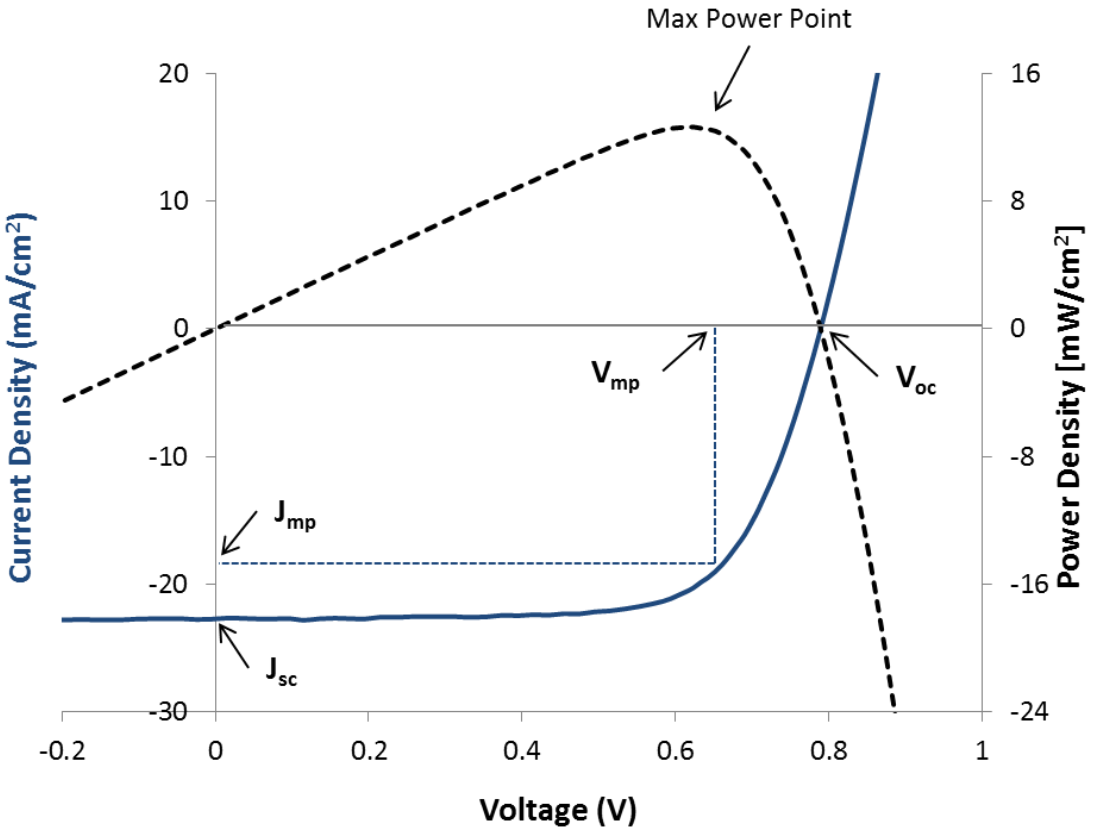

Figure 10B J-V curve of a CdTe cell with overlaid resulting power density, parameters V_{oc}, J_{sc}, V_{mp}, J_{mp} are identified.

$$FF = \frac{V_{mp} \cdot J_{mp}}{V_{oc} \cdot J_{sc}} \tag{1.1}$$

Efficiency (η) of the solar cell is calculated by comparing the power from 1 sun into the cell to the power generated by the cell at the maximum power point (Equation 1.2). The input power density is ~100mW/cm^2, and the cell in Figure 10B generates ~12mW/cm^2, therefore the resulting cell efficiency is 12%. The efficiency of a solar cell is directly related to the Voc, Jsc, and FF parameters of the cell and these characteristic parameters are commonly used to describe the ability of a photovoltaic cell in converting the solar spectrum to electricity.

$$\eta = \frac{P_{out}}{P_{in}} = \frac{V_{oc} \cdot J_{sc} \cdot FF}{P_{in}} \quad (1.2)$$

The PV market requires technologies that utilize large scale manufacturing of high efficiency modules. One of the most common direct-band gap, thin film solar cell materials is Cadmium Telluride (CdTe). CdTe has been expanding in the US PV market due to its manufacturability and optimum material properties. First Solar has demonstrated the ability to manufacture CdTe thin film solar cells at competitive costs (Figure 11) and has developed small area CdTe cells with efficiencies up to 17.3% [19].

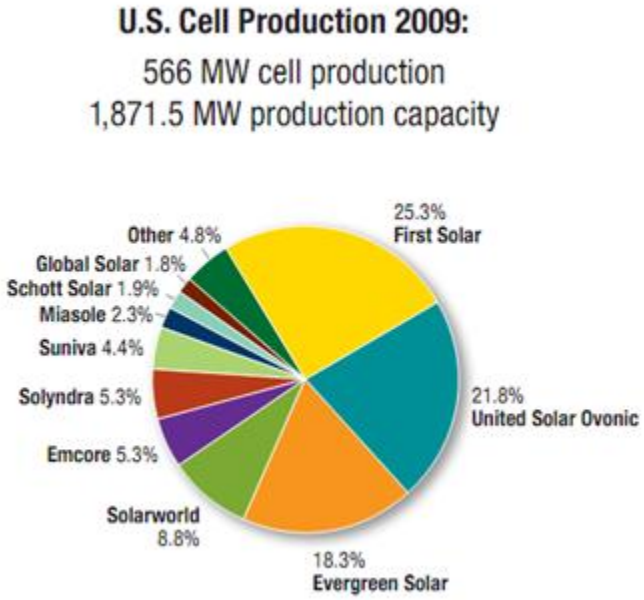

Figure 11 US solar cell production by company 2009 (US DOE, 2010) [8].

1.4 CdS/CdTe Solar Cell

The CdTe solar cell uses a hetero-junction formed by using n-type Cadmium Sulfide (CdS) as the window layer and p-type CdTe as the absorber layer. Cadmium sulfide has a band

gap of 2.4 eV, allowing a large percentage of the light spectrum to pass through it to the CdTe absorber. Cadmium Telluride has a band gap equal to 1.49 eV, which is near the optimum band gap for photovoltaics and is a direct band gap material, which minimizes the material required to absorb the light spectrum (Figure 5B) [20, 21]. Cadmium Telluride cells can be grown in two configurations, substrate and superstrate. In the substrate configuration (Figure 12B) the device is grown in the direction opposite to the way that the light would travel through the cell. The back contact surface is used as the structural support (Figure 12B). In the superstrate configuration the cell is grown in the direction the light would travel through the cell and a low absorbing glass and front contact is used as the structural support.

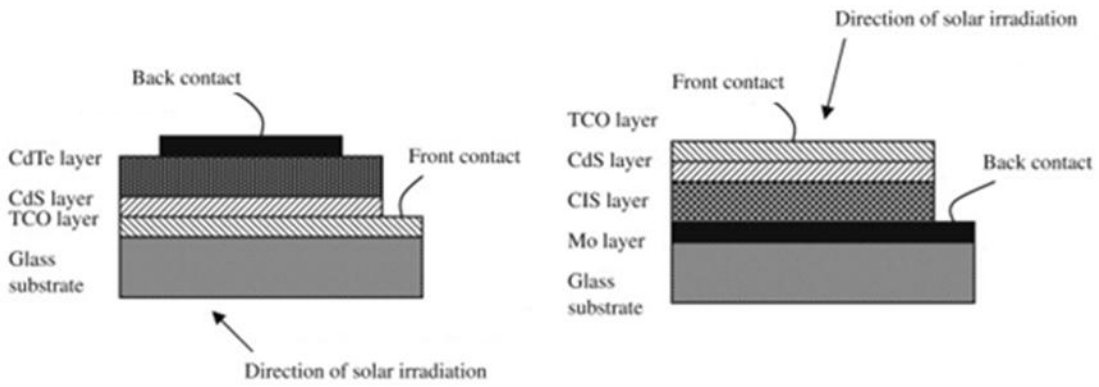

Figure 12 Schematic of PV Cells A: Superstrate configuration for CdTe B: Substrate configuration for CIS (Irvine, 2008) [22].

1.5 Formulation of the Problem

The highest efficiency cadmium telluride (CdTe) solar cells are produced using the superstrate configuration [19]. The first film deposited onto the glass is a transparent conductive oxide (TCO), which forms the front contact of the solar cell. The condition of the

TCO surface has an important impact on the quality of the other films comprising the cell. In particular, sputter treatments have been shown to reduce carbon contamination and modify the resulting interface between SnO_2 and CdS [23].

Poor growth regions, also known as pin holes, can form in the n-type CdS layer, allowing a shunt path to develop between the front contact and the p-type CdTe film [24]. Pinholes are particularly troublesome when a thin CdS layer is deposited on TCO-coated glass that has been cleaned using industry-standard techniques [25]. Figure 13A shows scanning-white-light-interferometry (SWLI) images of a CdS film deposited on TCO that was subjected to a standard cleaning process [26]. Even a small number of pin holes demonstrated in Figure 13A can cause a substantial decrease in fill factor (FF) and open circuit voltage (V_{OC}) [24].

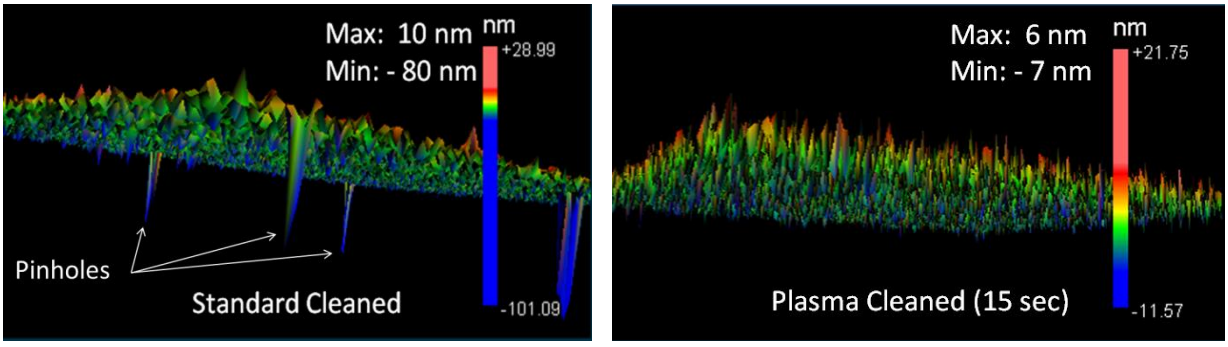

A B

Figure 13 Scanning-White-Light Interferometry of CdS films on standard-cleaned and plasma-cleaned TCO [26].

To minimize pinhole effects, relatively thick (100-200 nm) CdS layers must be deposited, resulting in a current density loss from absorption of light above the CdS band gap of 2.4 eV, and a current-density reduction as much as 4.6 mA/cm^2 [28]. Figure 13B shows a SWLI image of a CdS film that was deposited on TCO coated glass that was plasma treated for 15 seconds. No

evidence of pinholes was found on the plasma cleaned sample. The positive impact on cell performance of a plasma cleaning treatment will be explored in Chapter III. An alternative to thinning the CdS window layer is to increase the band gap of the CdS material and reducing loss from absorption in the window layer. The formation and impact to cell performance from a modified CdS window layer will be explored in Chapter IV.

Chapter II Experimental Details

2.1 Cell Fabrication

The CdS/CdTe solar cells studied here are manufactured by growing thin films using heated-pocket deposition sources that sublimate semiconductor materials within an in-line single-vacuum deposition system [29, 30]. The cells are manufactured on 3.6" x 3.1" Pilkington TEC 10 superstrates that consist of soda-lime-silicate glass, coated with a thin (30nm) intrinsic SnO_2 layer, a thin (20nm) SiO_2 film, and finally a thick (300nm) SnO_2:F layer as shown in Figure 14 [28]. Prior to plasma cleaning or film deposition, the TCO film is cleaned using a standard ultra-sonic detergent rinse, an ultra-sonic deionized water rinse, and finally an isopropyl alcohol wash. Plasma treatment can be done at this stage before the cell proceeds through the fabrication system shown in Figure 15. Here the deposition of the CdS and CdTe films occur and post-treatments with cadmium chloride and copper doping are performed. The plasma cleaning and film deposition processes are performed without breaking vacuum, and the samples are removed and carbon nickel layers are sprayed on for the back contact [29].

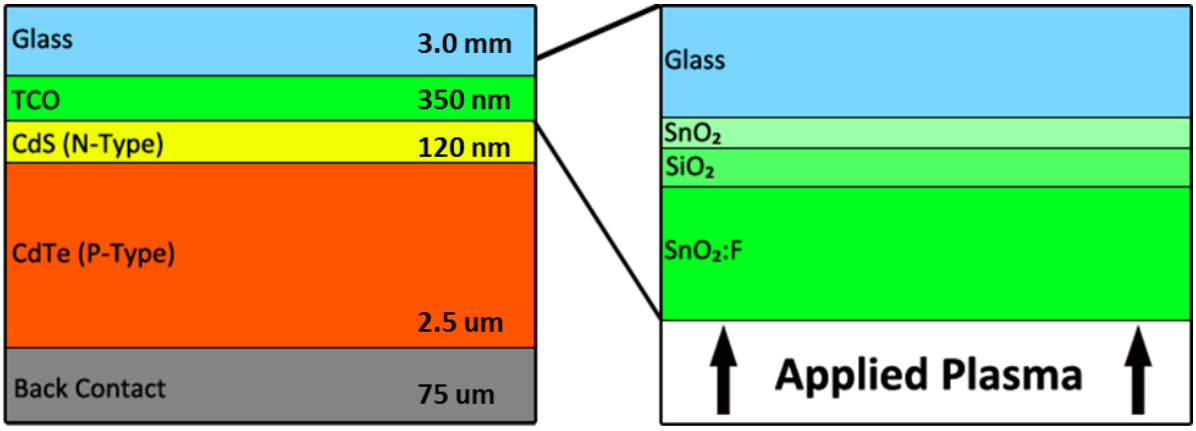

Figure 14 Structure of TEC 15 glass; Plasma-cleaning step at right.

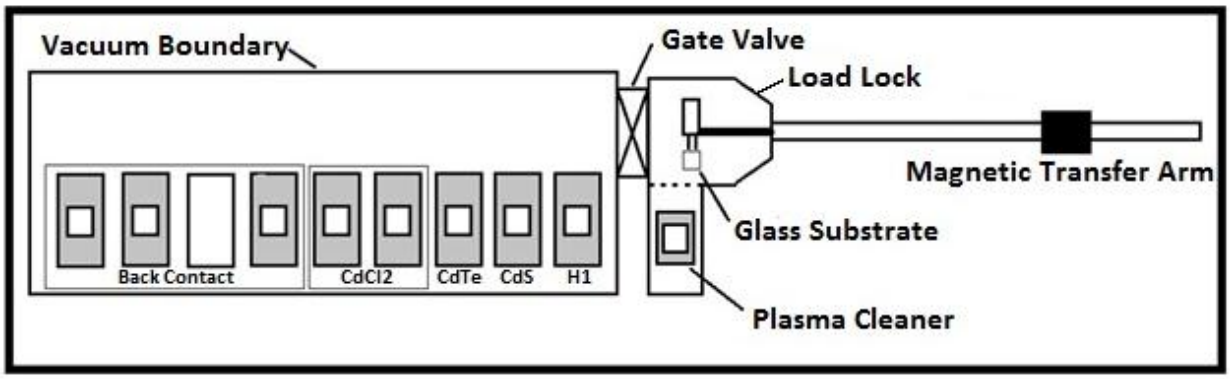

Figure 15 In-line single-vacuum deposition system at CSU for fabrication of CdTe cells [29].

2.2 Film and Device Characterization

Several methods are used to understand effects of the plasma cleaning treatment including material characterization and photovoltaic device characterization. Techniques presented in this thesis include Ultra Violet-Visible Spectrophotometry (UV-Vis), Contact-Angle Goniometer (CA), Scanning White Light Interferometry (SWLI), Atomic Force Microscope (AFM), X-Ray Photoelectron Spectroscopy (XPS), Scanning Electron Microscope (SEM), Energy-Dispersive X-ray Spectroscopy (EDS), Quantum Efficiency (QE), Current Voltage plots with optional temperature bias (JV and JVT), Electroluminescence (EL), and Light-Beam Induced Current (LBIC).

2.2.1 Ultra Violet-Visible Spectrophotometry

Ultra Violet-Visible Spectrophotometry (UV-Vis) is used to characterize the ability of a material to absorb, reflect, and transmit light as a function of the incoming photon wavelength. This is performed by utilizing multiple light sources and splitting the spectrum with a monochromator. In this research the spectrum wavelengths varied from 300 nm to 1000 nm;

which includes ultra violet, visible, and near infrared light. As the light is split, it is sent past an aperture and through the sample of interest (Figure 16). The beam is then captured by a photo detector that is cooled to 0^{o}C. Transmission versus wavelength data are recorded using a data acquisition system. This characterization technique provides data that can be used to identify the band gap of the different thin films used in CdTe cell manufacturing.

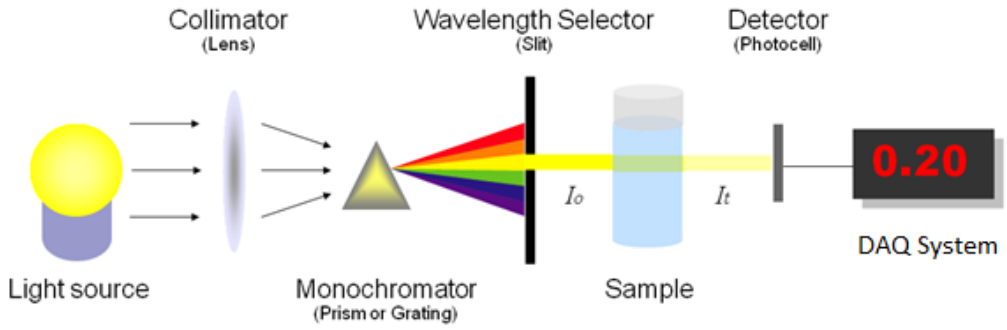

Figure 16 UV-Vis Spectrophotometry (Vo, 2011) [32].

2.2.2 Contact-Angle Goniometer

A contact–angle goniometer is a characterization tool that images the liquid–solid interface when a liquid droplet interacts with a solid surface in air (Figure 17). A drop of a liquid upon a solid surface assumes a lens shape controlled by three forces, the surface tension of the solid–vapor interface, the liquid–vapor interface, and the solid–liquid interface [33]. The contact angle is defined as the angle between the solid surface and the tangent to the surface of the drop at the point of contact. Contact angle measurements are extremely sensitive to contamination making this a powerful tool in measuring the relative cleanliness of a surface [34, 35]. Contaminants can prevent wetting on naturally hydrophilic surfaces, resulting in higher contact angles than desired. As a hydrophilic surface is cleaned of contaminants, the contact

angle will decrease and wetting improves (Figure 17) [36]. To generate a contact angle measurement, a deionized water droplet of a known volume is released from a dropper onto the surface. A camera is used to photograph the water droplet as it sits on the surface and a data acquisition system records the contact angle. For this research high contact angles on the TCO film suggest contaminates on the surface where pinholes could develop during CdS deposition and would lower cell efficiency.

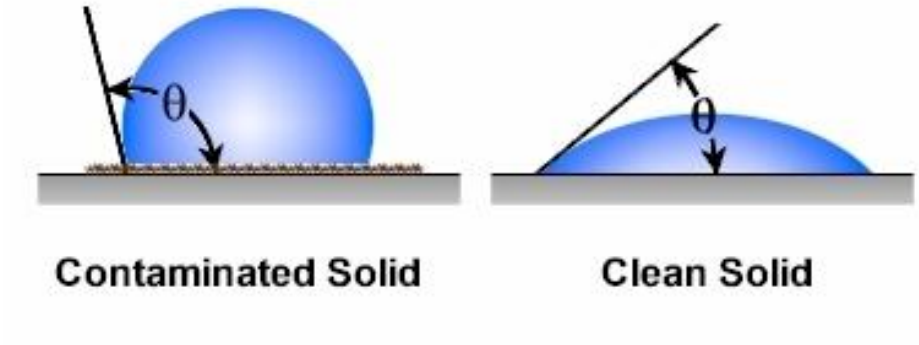

Figure 17 Contact-angle of contaminated and clean surface (Ramehart, 2012) [36].

2.2.3 Scanning White Light Interferometry

The Scanning White Light Interferometry (SWLI) is a characterization tool that allows for a non-contact mapping of surface roughness [33]. In this tool illumination from a white light source is filtered and focused to a beam that is sent to a beam-splitter where the light is directed to a reference mirror and the surface of interest. Interference bands form to create what are known as fringe patterns when the reference beam and light reflected from the surface are recombined (Figure 18). The fringe patterns are used to deduce the surface topography in software that converts these fringes to various height measurements. A

collection of height measurements made over the surface are used to form a 3D image of the surface. SWLI image resolution is ± 1 nm in the z direction (height) and ± 100 nm in the x-y direction (laterally). SWLI data are most useful in characterizing pinhole defects in the CdS film and thickness of CdS and CdTe films in the results presented in this thesis.

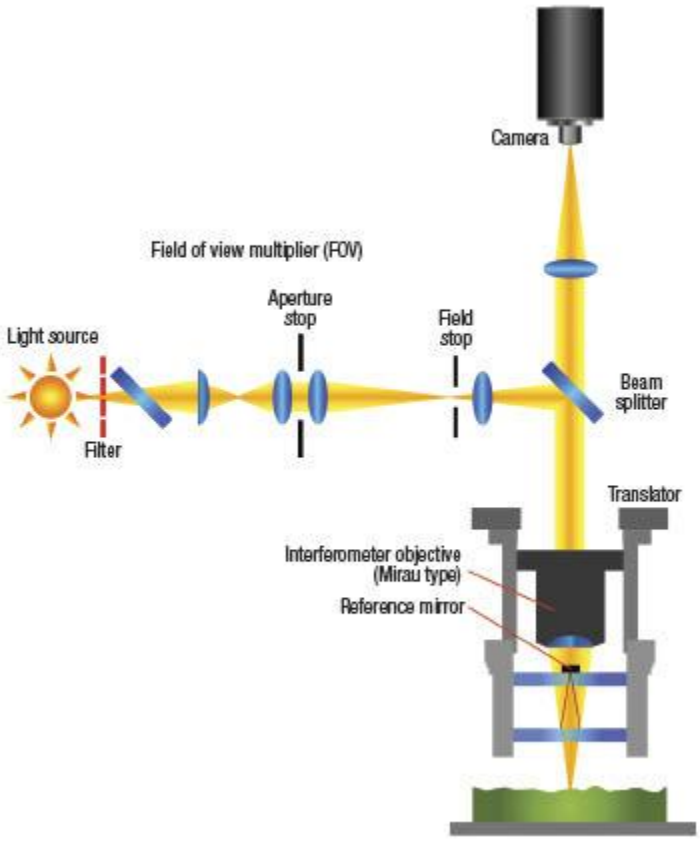

Figure 18 Schematic of a Scanning White Light Interferometer (Woods, 2009) [37].

2.2.4 Atomic Force Microscope

The Atomic Force Microscope (AFM) is a characterization tool used to resolve features of a surface on the atomic scale [38]. It operates using a cantilever beam that has a tip sharpened to a radius of 8nm near its free end (Figure 19). In this research images are

generated in the tapping mode of operation where the probe tip is not in contact with the surface but oscillating at ~170 kHz about 100-200 nm above the surface. This method requires no direct contact with the surface, which reduces the risk of tip damage or build up of liquids on the tip that can be transferred from a surface being characterized. As the probe oscillates along the surface, forces such as Van der Waal and dipole-dipole interactions cause the cantilever frequency to change. To measure the oscillating frequency of the cantilever, a spot size laser beam is reflected from the top of the cantilever to a stack of photodiodes. A 3D image of the surface is generated as the probe tip is scanned back and forth across the region of interest.The AFM technique allows for high lateral resolution (± 10nm) images of TCO films to be generated after various plasma cleaning procedures have been performed.

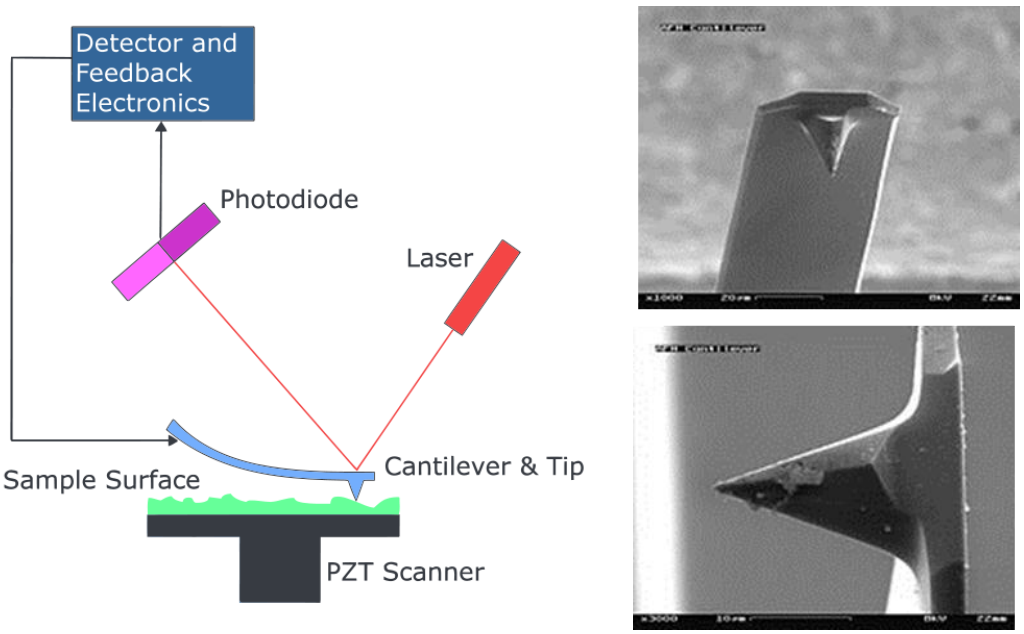

Figure 19 A: Block diagram of Atomic Force Microscope, B: SEM images of AFM tip at 100 um scale (Top) and 30 um scale (Bottom) (Wiki, 2012) [39].

2.2.5 X-Ray Photoelectron Spectroscopy

X-ray Photoelectron Spectroscopy (XPS) is one of the most widely used techniques for elemental analysis of the near surface region, giving insight into the material's surface chemistry [40, 41]. This is performed by bombarding the surface of the sample with x-rays to release electrons from a wide range of valence band locations. The relative number and energy of the electrons are measured using an electro-static analyzer (Figure 20). The difference between the x-ray energy and the energy of the freed electron is a measurement of the binding energy of the electron. A graph is populated by counting the number of electrons vs. their binding energy. Each element and its local bonding environment have characteristic sets of XPS peaks, which can be referenced to identify elements and their chemical relationship between nearby atoms. In addition, XPS can be paired with an ion source to sputter etch away layers of material from the sample in between XPS spectra measurements, generating a depth profile through a sample. In this thesis, XPS measurements are used to identify materials and their chemical states after being deposited using plasma assisted deposition processes.

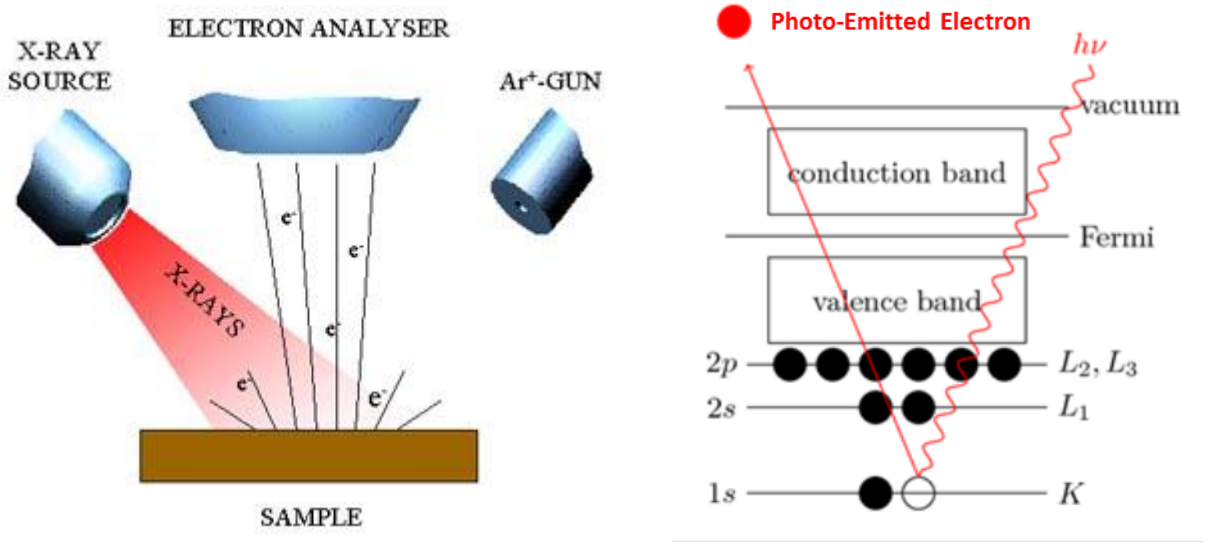

Figure 20 Diagram of XPS (Laurin, 2009) [42, 43].

2.2.6 Scanning Electron Microscope

A Scanning Electron Microscope (SEM) uses electrons instead of photons to enable high magnification images to be obtained. This is performed by generating an electron beam using a filament, generally tungsten, which is focused to a small spot size (Figure 21). The spot size is on the order of nanometers in diameter when it strikes the surface being imaged. As the electron beam interacts with the material secondary electrons are produced and emitted from the surface along with x-rays. The secondary electrons are collected by detectors located near the specimen as the electron beam is scanned over the surface. High resolution images are generated by combining the detectors output with locations where the electron beam was scanned [44]. A JOEL JSM-6500F microscope was used to image specimens at an operation voltage of 15kV. The SEM allowed visual assessment of material surfaces and these images were used to identify changes in grain size and material structure.

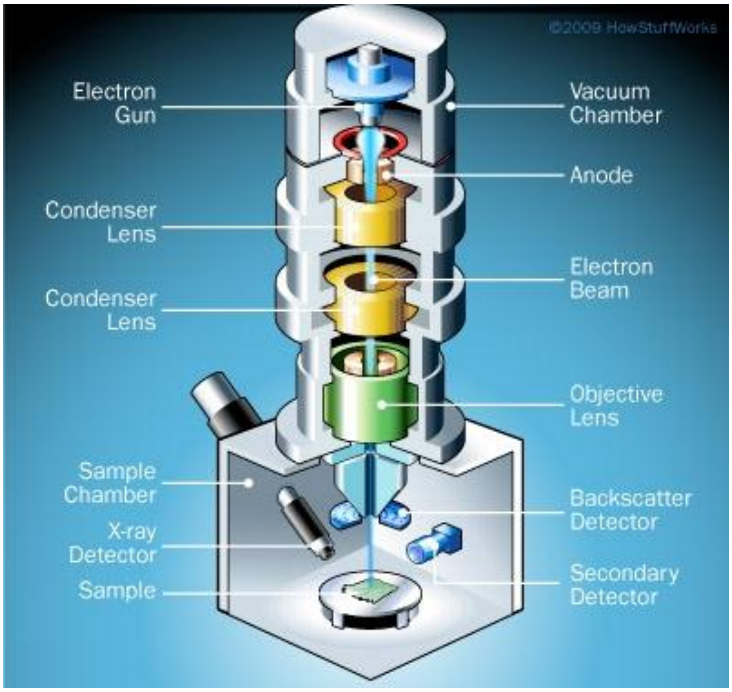

Figure 21 Cross section of an SEM (Atteberry, 1998) [45].

2.2.7 Energy-Dispersive X-ray Spectroscopy

Energy-Dispersive X-ray Spectroscopy (EDS) is an analytical tool for characterizing the elements present in a material, and is generally used in combination with an SEM. When an SEM electron beam bombards the surface of a sample, an electron can be ejected from an inner shell. This creates a vacancy in the shell, allowing an electron from a higher shell to fall down into the vacant shell, releasing an x-ray with energy equal to the difference between the two shell states (Figure 22). These x-rays are detected and tabulated in plots of X-ray counts vs. energy. Since every element has a characteristic x-ray energy, EDS data is used to identify elements and their relative concentrations within the sample. EDS is used in this research to identify the presence of elements of interest within a film following plasma enhanced deposition techniques.

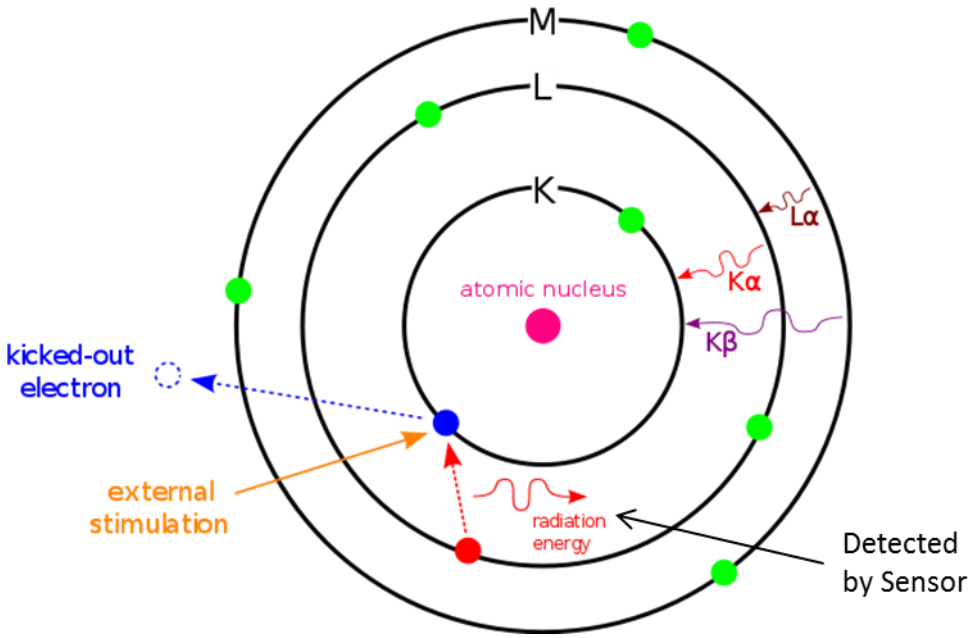

Figure 22 Principle of EDS (Wiki, 2012) [46].

2.2.8 Quantum Efficiency

The quantum efficiency (QE) identifies the percent of hole-electron pairs extracted from a photodiode for every incident photon of a given energy. QE data is typically presented in graphs of conversion percent as a function of wavelength. Detailed analysis of the QE spectrum can identify film thickness, short circuit current, and band gap. QE data can also provide insight into the losses in a device (Figure 23A). Losses that can be identified include absorption in the glass, TCO, and CdS layers along with reflection and deep penetration losses. QE data are generated by sending white light from a 1 sun replicating light source toward a monochromator. Here the light beam is split in its varying wavelengths; the monochromator was used to select wavelengths from 400 to 900 nm in this research. The beam leaving the monochromator is chopped at a set frequency and focused onto the solar cell. Current produced by the cell from the light at the selected wavelength is detected by a preamplifier

where the current is converted into a signal that a lock in amplifier measures at the chopper frequency (Figure 23B). This method yields a current (hole-electron yield) vs. wavelength (photon energy) graph for the cell (Figure 23). QE measurements require a calibrated reference device, and the results presented in this thesis use a Gallium Arsenide solar cell calibrated at the U.S. National Renewable Energy Laboratory.

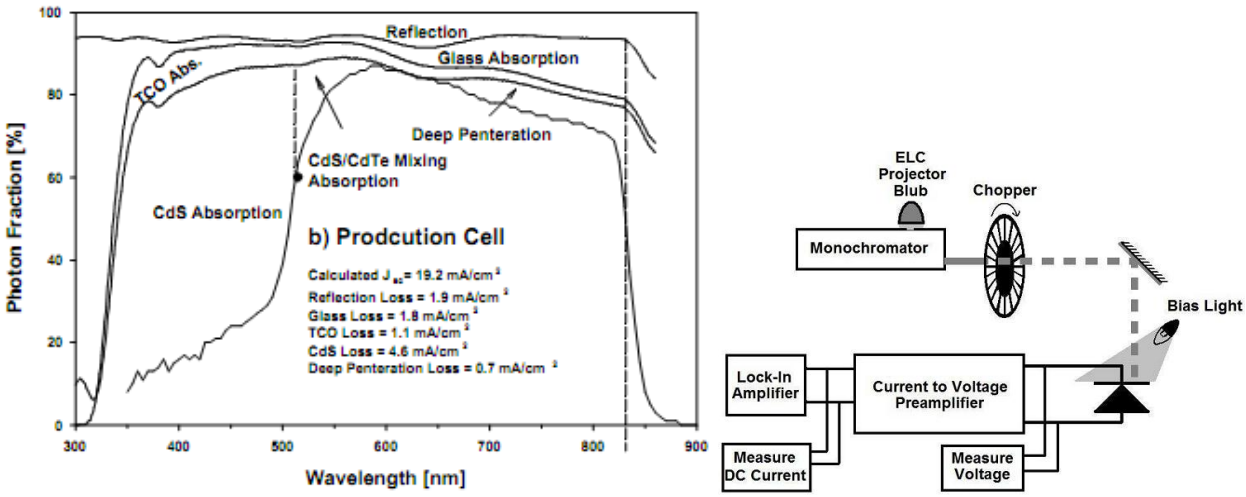

Figure 23 A: Quantum efficiency plot of a CdS/CdTe Cell B: Schematic diagram for QE measurement (Demtsu, 2005) [28], (Nagle, 2007) [47].

2.2.9 Current-Voltage Measurements

Current-voltage (J-V) plots are common measurements to characterize a photovoltaic cell. As described in Section 1.3, this technique measures cell operation parameters: V_{oc}, J_{sc}, FF and efficiency to describe the quality of a solar cell. Measurements consist of applying light that approximates the spectrum from the sun at the surface of the earth. This thesis utilizes a spectrum standardized to 1.5 air mass units (AMU). Figure 24A compares the AMU 1.5 spectrum to the spectrum generated by the xenon arc lamp used in this research. The graphs

are generated by applying a range of biases to the cell and measuring the resulting current generated. A typical current density vs. voltage plot is shown in Figure 10B. Cell performance varies with temperature, and tests were conducted on cells heated with a heat gun and cooled with liquid nitrogen to obtain J-V plots as a function of temperature (JVT). This device characterization method is the most common characterization technique used to understand the quality and performance of cells. This method is utilized in this research to show the difference between plasma cleaned and standard cleaned TCO devices and to show improvements induced from plasma enhanced processing of CdS films.

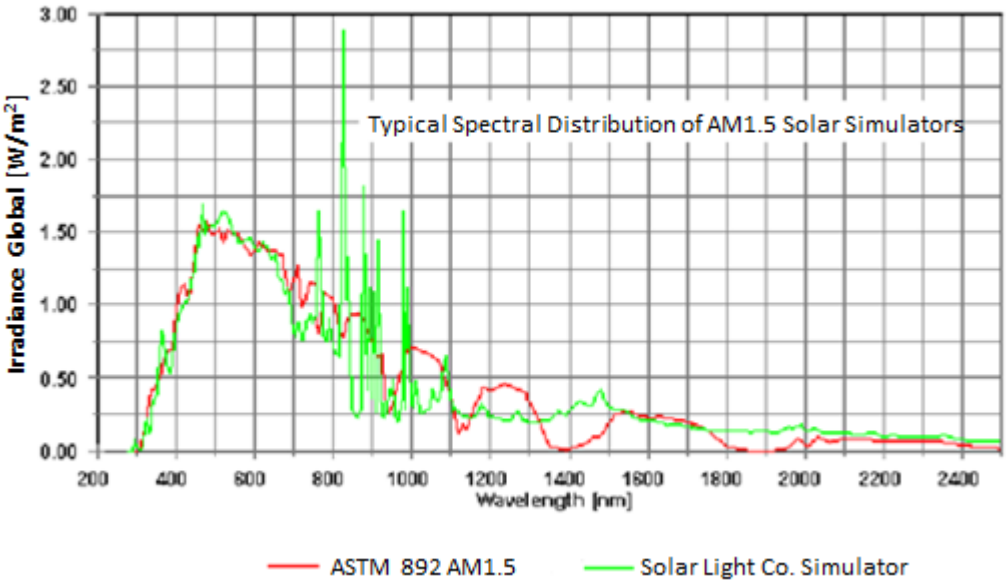

Figure 24 A: AMU 1.5 Spectrum vs. Light source spectrum B: J-V plot of a CdTe cell (Davies, 2008) [24].

2.2.10 Electroluminescence

Electroluminescence (EL) exploits the reciprocity relationship between solar cells and light emitting diodes (LEDs) to take fast, spatially-resolved measurements of a device (Figure 25). EL

is performed by placing a cell in a light controlled environment with the cell in forward bias at a current of 20 mA/cm², which is similar to typical J_{sc} values. Images of the cell are then taken by a silicon CCD camera cooled to -25 °C. EL data give insight into cell uniformity as well as its relation to Voc [48].

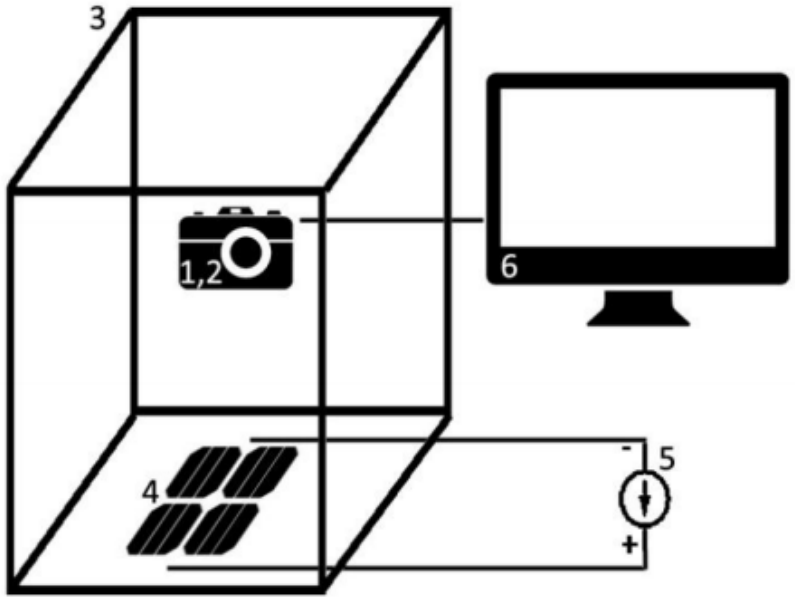

Figure 25 Basic El setup: (1) CCD camera, (2) interchangeable lenses, (3) enclosure, (4) sample, (5) current source, and (6) computer (Raguse, 2012) [48].

2.2.11 Light Beam Induced Current

Light beam induced current (LBIC) measurements produce a spatial map of quantum efficiency. A light is provided by an electrically modulated laser diode operating at 638-nm. A set of optics is used to direct and focus the laser beam onto the cell where an electrical signal is measured using a lock-in amplifier (Figure 26) [49]. As the sample is moved under the laser spot

a map is produced over a user defined area with resolution of 1, 10, or 100 µm. The LBIC mapping can be done at short circuit conditions or with a voltage bias applied.

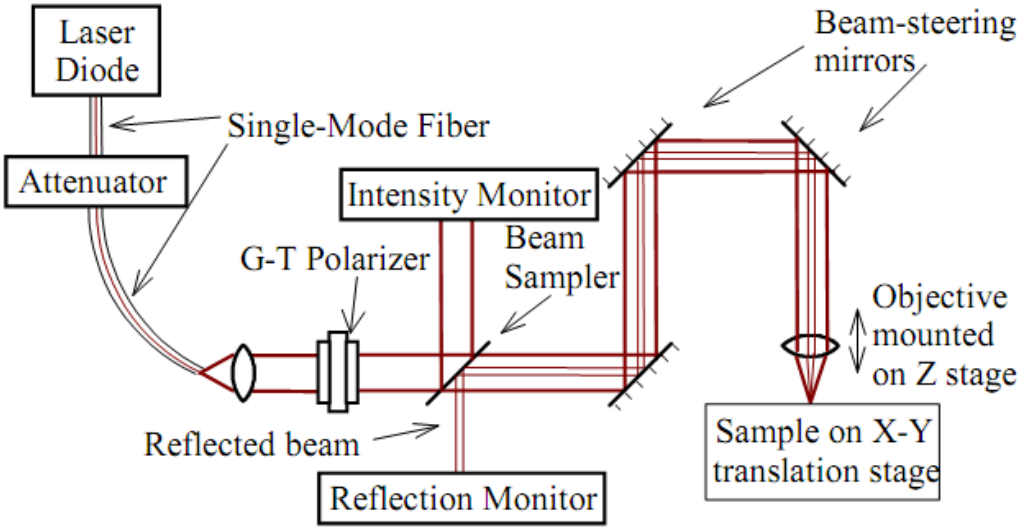

Figure 26 Schematic of LBIC apparatus (Hiltner, 2001) [49].

2.3 Conclusion

The characterization techniques described in this section were used to study materials and cells deposited in an inline manufacturing tool for producing CdTe solar cells. The samples and controls were tested for various material properties and device performance parameters to create comparisons between plasma cleaned and standard cleaned substrates and between CdS window layers created with and without Plasma Enhanced Close Space Sublimation. Material analysis of the CdS and TCO material is done using contact angle, AFM, and SWLI. Device performance is described with QE, J-V, and J-V-T; with more detailed device characterization of uniformity measured with EL and LBIC. PECSS generated CdS:O films are

characterized using use UV-Vis, XPS, SEM, and EDS, along with device performance characterization by QE, and J-V.

Chapter III Plasma Cleaning

3.1. Introduction to Plasma Cleaning:

This chapter will discuss the use of hollow cathode plasmas as a technique to clean the surface of TCO-coated glass substrates, allowing for higher quality CdS films to be deposited. Plasma environments are complex and chemical surface reactions can occur in combination with physical etching of a substrate [50, 51]. If performed under suitable conditions the surface can be cleaned quickly by ion bombardment. Oxygen (molecular and atomic) ions formed throughout the discharge are chemically reactive and enhance the cleaning action. Although oxygen plasma is highly reactive, interaction with the graphite walls of the source does not significantly affect the lifetime of the source [52, 53].

Current-Voltage (JV), Quantum Efficiency (QE), Electroluminescence (EL), and Light-Beam Induced-Current (LBIC) measurements are used to characterize the differences in the devices made from plasma cleaned and standard cleaned TCO substrates. QE was used to calculate CdS thickness from the Beer-Lambert Law and to quantify the blue photon generated current. Both CdS thickness and blue-photon current were found to be affected by plasma cleaning treatment. In addition, maps generated by scanning white-light interferometry (SWLI), electroluminescence (EL), and light-beam-induced current (LBIC) all show uniformity improvements with plasma cleaning treatment.

3.2 Plasma Cleaner Hardware and Treatment:

The plasma cleaning treatment is performed using a hollow cathode plasma discharge integrated into a heated pocket deposition (HPD) source [29, 26, 54]. It is noted that a HPD source is similar to a close space sublimation (CSS) source. Two anode configurations were used to drive the hollow cathode discharge (Figure 28). One anode design utilized a single tungsten wire spanned across the graphite source (Figure 28B). As described by Gueroult et al. [55], a wire-anode plasma source is a type of low-pressure, hollow cathode gas discharge where the electron mean free path exceeds the discharge chamber length scale, electrostatically confining the electrons. The wire-anode configuration enables low pressure (40-400 mTorr) gaseous discharges to be sustained at low applied voltage (~300-500 V) within a source with a characteristic dimension of a few centimeters. The top surface of the plasma discharge is contained by the TCO-coated glass substrate. In parallel with this plasma cleaning study on solar cell effects, Metz [54] has performed experimental characterization of the plasma properties within the plasma cleaner.

The TCO coating on the glass has a fluorinated tin oxide conductive coating (Figure 14), which is grounded to the walls of the graphite source. Ions are formed within the plasma source at a potential close to the wire anode, and they accelerate from this potential to the cathode potential through a thin sheath that separates the bulk of the plasma from the pocket walls and the TCO-coated glass substrate. For our operating conditions the acceleration process within the sheath is collisionless, and hence, the ions strike the substrate with energy close to the anode-cathode potential difference. The ion bombardment removes contaminates via both

physical and chemical etching and the removal of chemisorbed oxygen from the TCO surface [56]. Plasma density and electron temperature have been measured within the source to be between 10^{15}–10^{16} m^{-3} and 0.5-1 eV, respectively, depending upon operating pressure, gas composition, and discharge power setting [54]. Over these operating conditions, discharge voltage and ion bombardment current density vary from 350-450 V and 0.05 – 0.8 mA/cm^2, respectively.

The wire anode configuration was found to be undesirable for several reasons. For instance, the wire location resulted in thermal non-uniformity on the TCO substrate. In addition, the non-graphite wire composition allowing for possible contamination, and the small diameter anode wire made the source difficult to maintain and repair. To address these issues, the discharge source was redesigned with plate anodes. The plates were manufactured from graphite and placed inside the wall of the source pocket (Figure 28A). This configuration produced similar plasma characteristics to the wire anode [54]. Figure 27 shows that the plate anode operates at discharge voltages ~75 V greater than the wire anode over a pressure range from 50 to 200 mTorr.

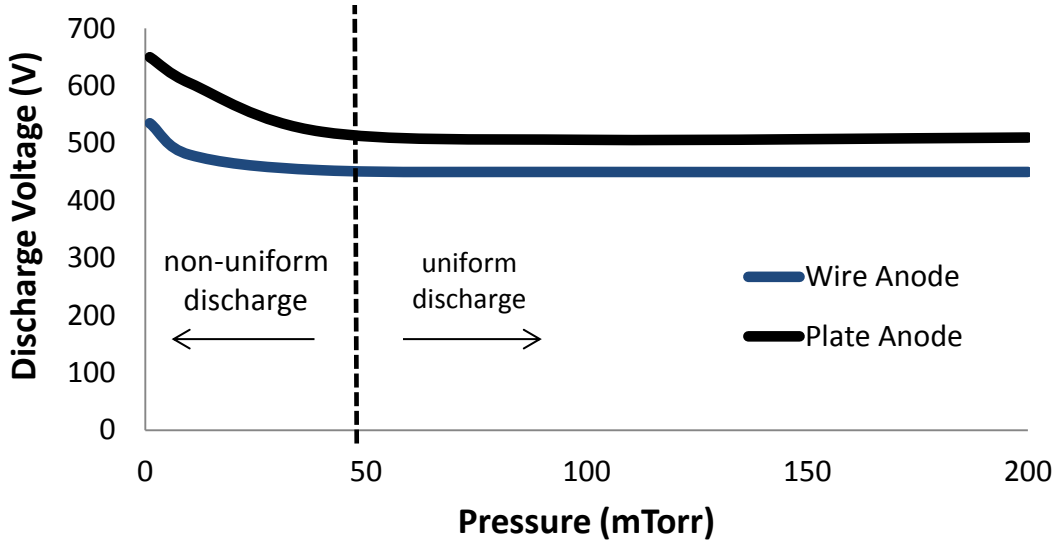

Figure 27 Comparison between wire and plate discharge voltage at various background pressures.

The initial neutral pressure condition of 40 mTorr for the plasma cleaner was established by the process conditions used in the current cell manufacturing process. However through visual uniformity, ease of ignition, and power supply voltage limitation for ignition, a higher pressure of 200 mTorr was selected for operation of the plasma cleaner. An inline plasma cleaner bay was incorporated into the load lock of the single-vacuum CdTe solar cell manufacturing chamber to allow for plasma cleaning at 200 mTorr (Figure 15). The power supplied to the plasma source was determined by the lowest discharge current that yielded visual uniformity. This operation condition of 0.22 mA/cm^2 (~400 V) for 30 sec in an N_2O_2 (2% O_2) back ground gas was maintained for all preliminary testing. Once full device characterization testing was initiated, the plasma cleaning discharge power was varied to determine an effective plasma cleaner current density of 0.11 mA/cm^2. Assume preliminary operation parameters unless otherwise stated.

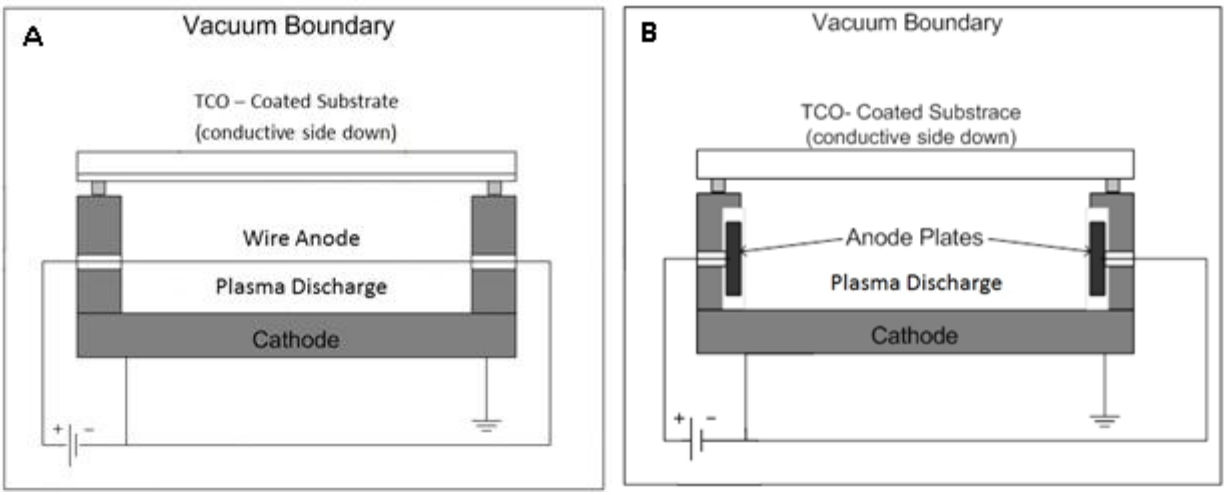

Figure 28 Hollow-cathode glow discharge integrated into a source design for plasma cleaning, A: Wire anodes, B: Plate anodes.

3.3 Results and Discussion

The hydrophobicity of the TCO films were measured using a deionized water contact angle goniometer. The first image in Figure 29 is a droplet placed on a substrate that had undergone a standard cleaning process, which includes a detergent rinse, deionized (DI) water rinse, and an isopropyl alcohol (IPA) rinse. Note that the detergent and DI water rinses where performed in an ultrasonic cleaner. The second image is of a substrate that underwent the standard cleaning process and then was exposed to plasma for 30 sec. The plasma cleaned surface resulted in an immeasurably low contact angle, this hydrophilic behavior suggests improved removal of contaminates from the surface. It is expected that contaminates left over from manufacturing and handling of the substrates are not completely removed by the industry standard cleaning process and require a further plasma cleaning to be remove.

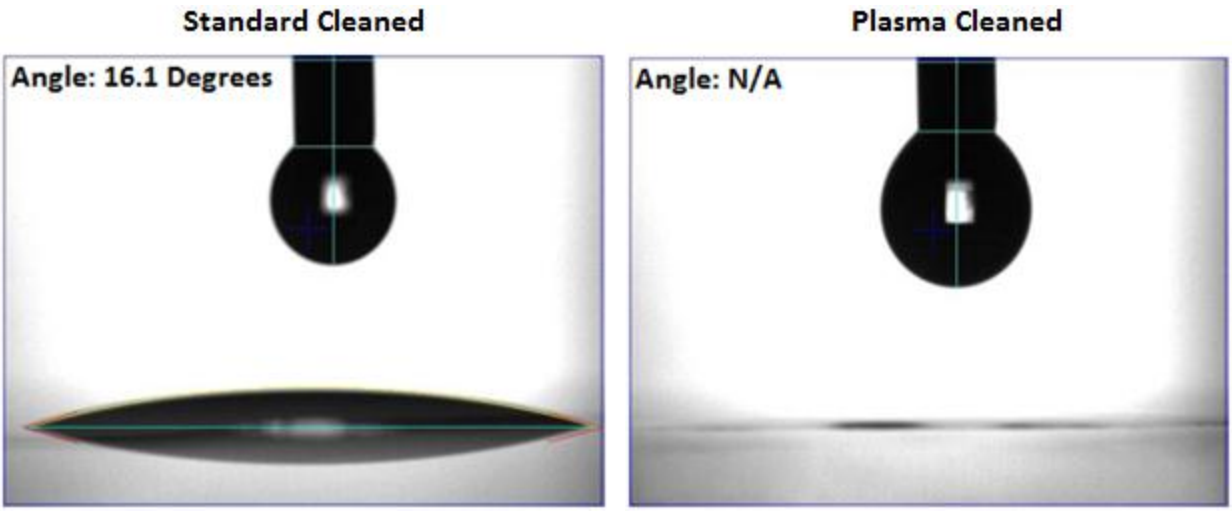

Figure 29 Contact angle on standard cleaned and plasma cleaning TCO.

Figure 30 shows AFM images of the TCO after a standard cleaning, a 0.11 mA/cm^2 plasma cleaning (30 seconds), and a 0.44 mA/cm^2 plasma cleaning treatment (30 seconds). AFM images show a slight increase in surface roughness upon a low current density treatment of 0.11 mA/cm^2. With an increase in plasma cleaning current density to 0.44 mA/cm^2 there is no continued increase in roughness (Table 1). This increase in surface roughness suggests an ion etching effect to the surface.

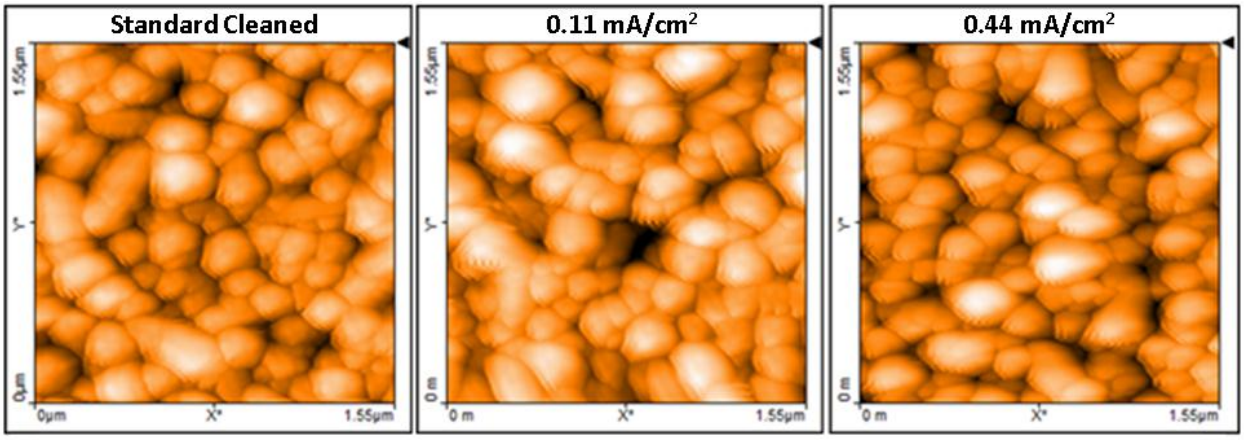

Figure 30 AFM of standard and plasma cleaned TCO samples.

Table 1 Roughness values for Figure 31 AFM images.

Film	TCO	TCO	TCO	
Plasma Treatment Current Density	0.0	0.11	0.44	mA/cm^2
RMS Roughness	**14.619**	**16.835**	**16.849**	**nm**
Average Roughness	11.82	13.564	13.27	nm

If an aggressive plasma cleaning treatment is preformed the transmission of the TCO film is affected. As Figure 31 shows, with an increasing treatment time or current density a decrease in transmission across the 300-650nm spectrum develops. This is hypothesized to be a result from the preferential sputtering of the SnO_2:F film, leaving behind a tin rich surface resulting in the reduction of transmission. However the utilized plasma cleaning treatment discussed below is well below these aggressive treatments and result in no measurable change in TCO transmission.

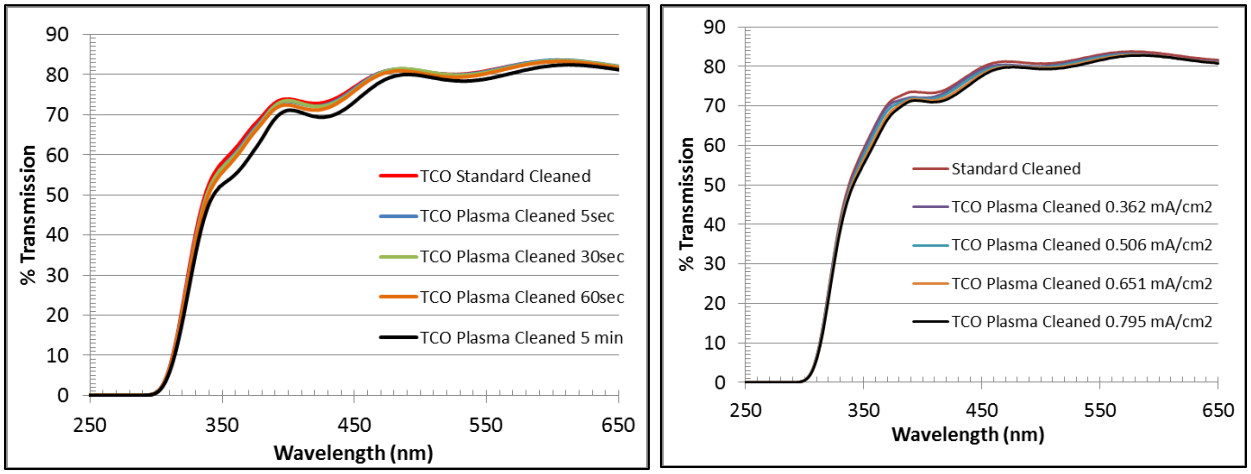

Figure 31 UV-Vis Transmission of TCO films at varying A: Plasma treatment time B: Plasma current density.

CdTe cells typically maintain a nearly constant V_{oc} when CdS thickness is greater than a given value, but significant decreases in V_{oc} and loss of cell efficiency below that value. Figure 32 shows the amount of blue current (from photons with energy above the CdS band gap, ~500

nm) and the corresponding V_{OC} from a set of cells with varying CdS thickness. At CdS thicknesses below approximately 90-110 nm, the cells experience a reduction the V_{oc} that dominates the cell efficiency. This results in an optimum CdS thickness where V_{oc} has not shown a significant decrease and current loss due to blue light (CdS) absorption is low.

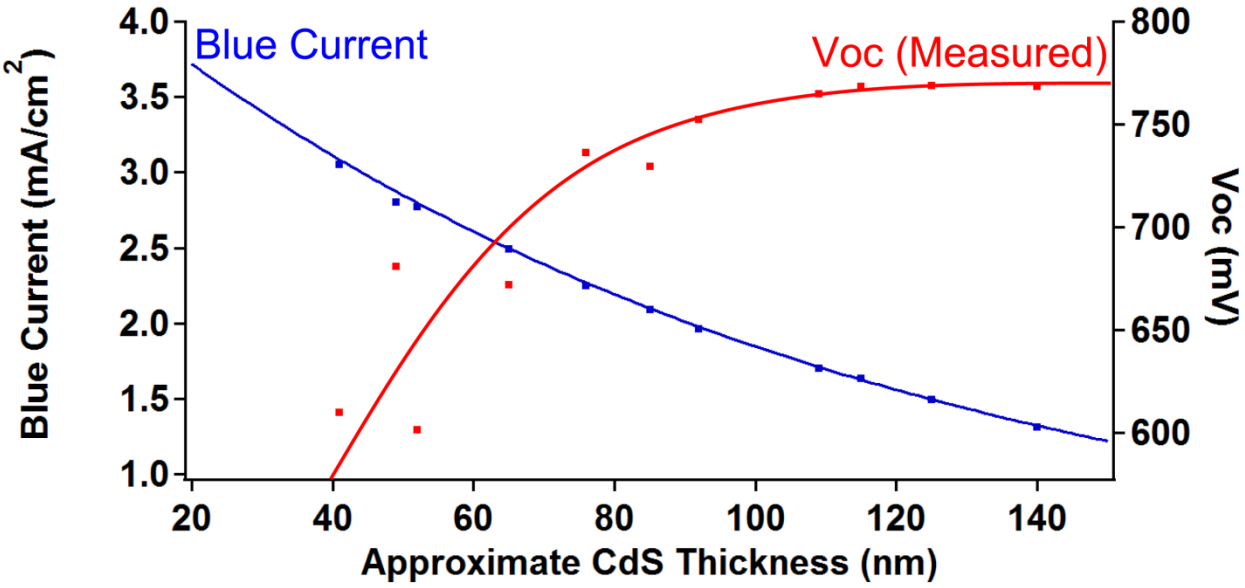

Figure 32 Open-circuit voltage and short-circuit current density vs. CdS thickness.

The current density used for plasma cleaning affects the CdS thickness (Figure 33). When a low plasma current density (dashed red line) is applied, the thickness of the CdS is less than on the adjacent cell without plasma cleaning, as shown by increased blue photon quantum efficiency response in Figure 33. With larger plasma-cleaning current densities, the CdS thickness increases gradually (dotted red line) and eventually surpasses the standard treatment thickness (solid red line). There is not a good explanation for the variation in CdS thickness with

the aggressiveness of the pre-deposition plasma cleaning. What is clear is that even with thinner CdS following plasma cleaning, the cell voltage is increased, as described below.

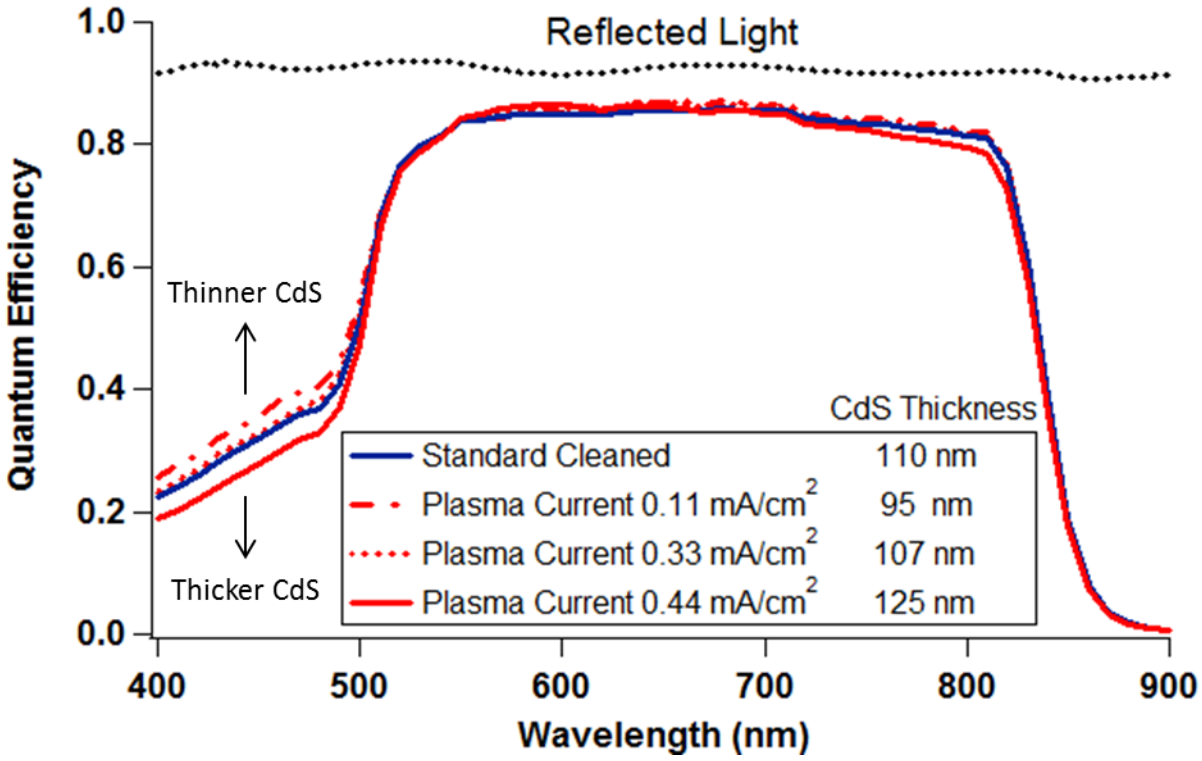

Figure 33 QE at varying plasma cleaning treatment current densities.

For a direct comparison of cells with and without plasma cleaning, Figure 34 shows two cells where the CdS deposition time was adjusted so that both CdS thicknesses are very close to 65 nm (which is in the region of decreasing V_{oc} as shown in Figure 32). The two cells had a nearly identical J_{sc} of 24 mA/cm^2. The voltage of the plasma treated device, however, was 80 mV greater than the standard-treated device at this CdS thickness.

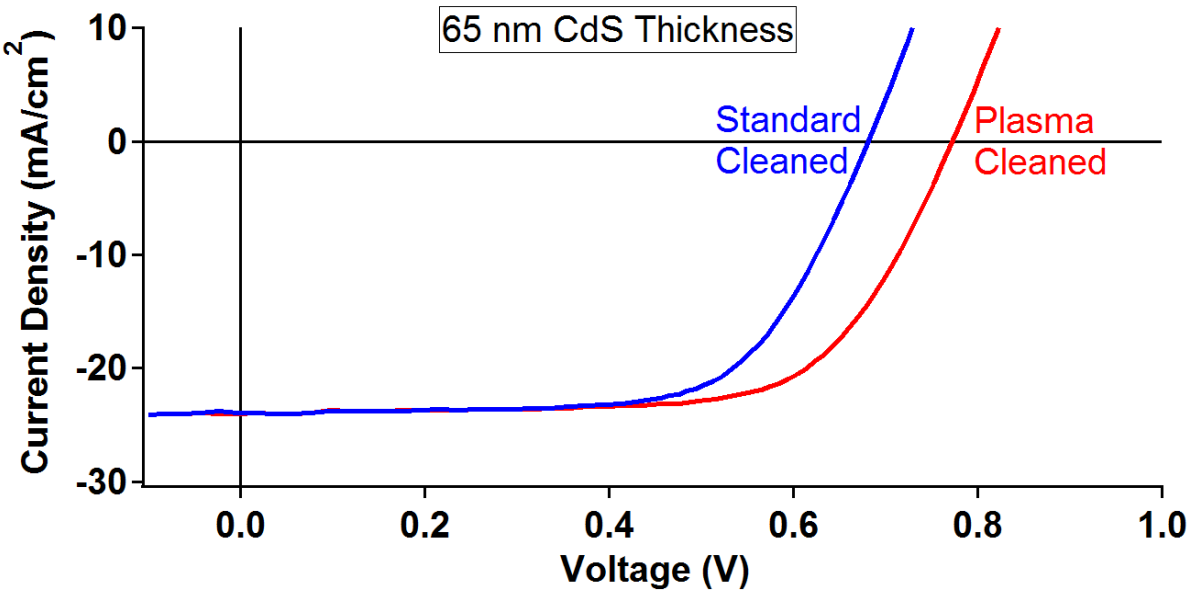

Figure 34 J-V Curves of standard and plasma cleaned TCO at a CdS thickness of 65 nm.

There are cell-to-cell variations in how much current and voltage increases when low current plasma cleaning is employed. In all side-by-side comparisons, however, the plasma-cleaned cells had both higher current and higher voltage. Figure 35 demonstrates voltage and efficiency for a broad range of cells produced with and without plasma-cleaned TCO. The standard cleaned TCO cells begin to degrade in Voc at around 90-110 nm, while the plasma cleaned TCO cells maintain V_{oc} down to 60-70 nm. The cell efficiency difference between plasma cleaned and standard cleaned near 65 nm was 1.6 % absolute. At larger CdS thicknesses above 100 nm, the plasma cleaning treatment shows only marginal increases in cell performance compared with standard cleaning. Note that CdS thicknesses above 100nm result in lower cell efficiency due to decreased current from CdS. At thicknesses below 100nm, cell efficiency drops due to decreasing V_{oc} as discussed above.

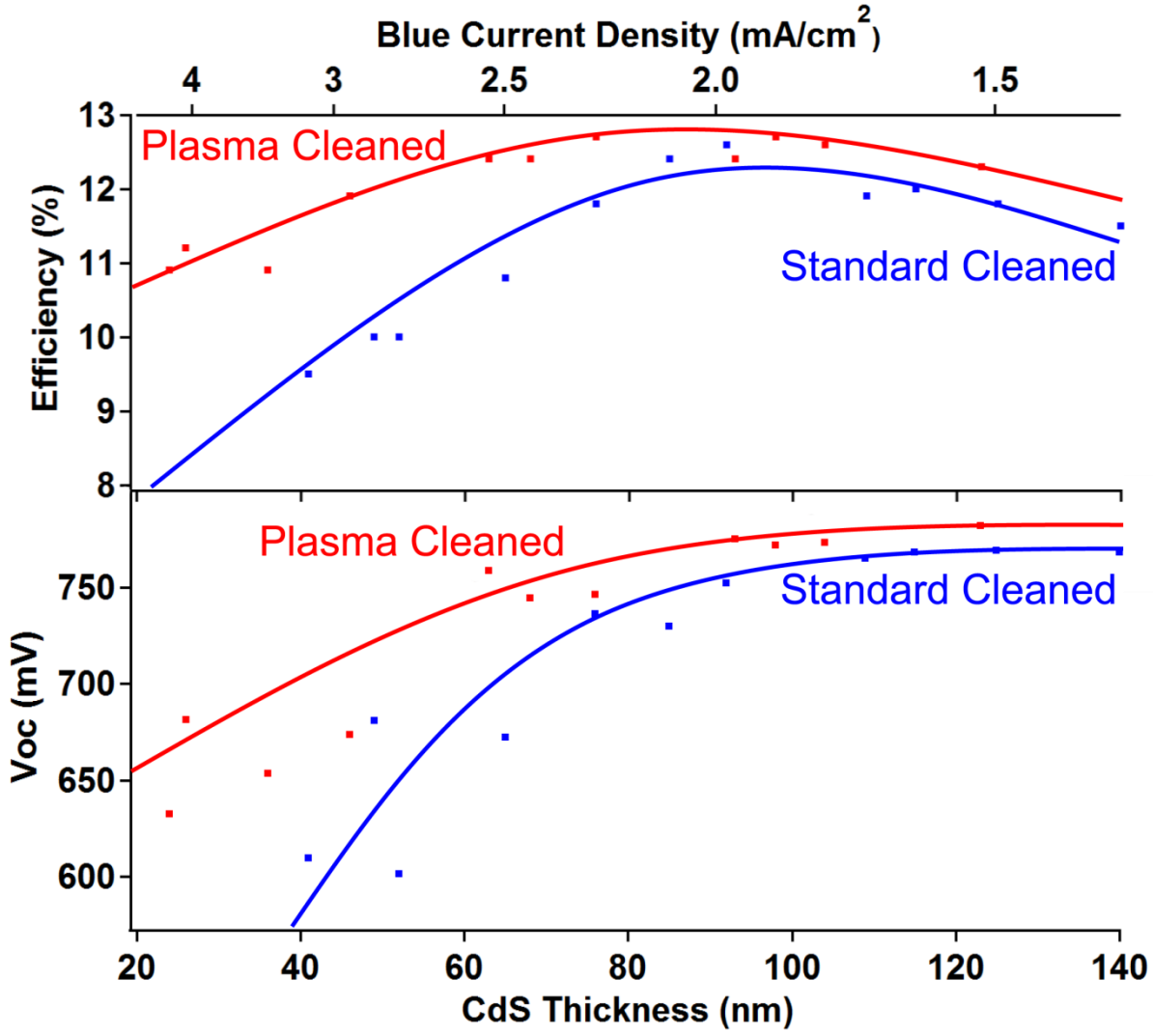

Figure 35 Open-circuit voltage vs. CdS thickness at plasma cleaned and standard cleaned conditions.

Further J-V investigation of the cells in Figure 34 reveals a constant offset of V_{oc} over a range of temperatures. Figure 36 shows that the y-intercept, or built-in-voltage of the plasma-cleaned cell, is improved to a value approximately equal to the CdTe band gap. This improvement can be attributed to the removal of pinholes between the TCO and p-type CdTe. The parallel slopes imply no other significant effects.

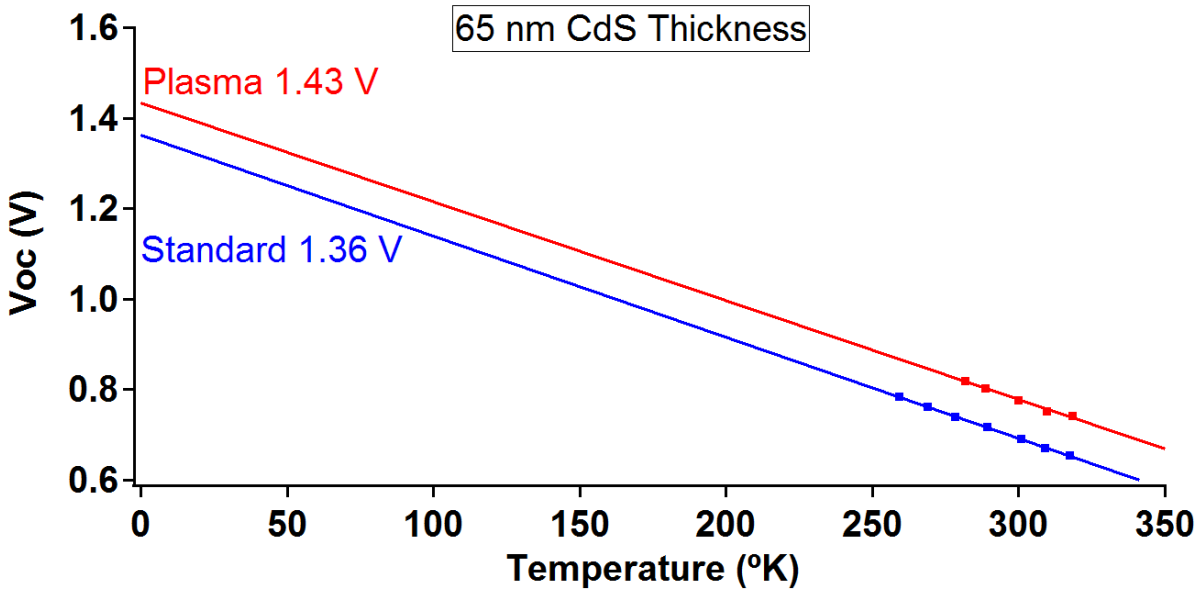

Figure 36 Temperature depended JV for plasma and standard cleaned TCO Parameter.

Table 2 gives a summary of representative cells with three different categorized CdS thicknesses, a thick (120nm), thinner (105nm), and thinnest (65nm) condition. At these three CdS thicknesses devices generated on standard cleaned and plasma cleaned TCO's are compared. Note that the cells with each categorized cells have are nearly the same thickness. As expected, in each category the current density is also nearly the same, however fill factor is increased after plasma cleaning, and the voltage is significantly increased for thinner CdS after plasma cleaning.

Table 2 Comparison of performance parameters at varying CdS thicknesses.

Parameter	Thick		Thinner		Thinnest	
	Standard Cleaned	Plasma Cleaned	Standard Cleaned	Plasma Cleaned	Standard Cleaned	Plasma Cleaned
CdS Thickness (nm)	125	123	109	104	65	63
Voc[V]	0.775	0.782	0.774	0.79	0.681	0.772
JV Jsc[mA/cm^2]	22	22.4	22.3	22.7	23.9	24.0
Blue Jsc[mA/cm^2]	0.84	0.88	1.11	1.2	2.18	2.24
Fill Factor[%]	69.2	70.3	69	70.5	66.6	67.3
Efficiency[%]	11.8	12.3	11.9	12.6	10.8	12.4

Electroluminescence (EL) intensity correlates well with cell voltage for CdTe [48]. Figure 37 shows a side by side comparison of the EL performed on the cells in Table 2. It is clear that the plasma-cleaned cells have a larger and more uniform EL signal. This agrees with the higher V_{oc} measured by J-V and suggests a more uniform growth of the device.

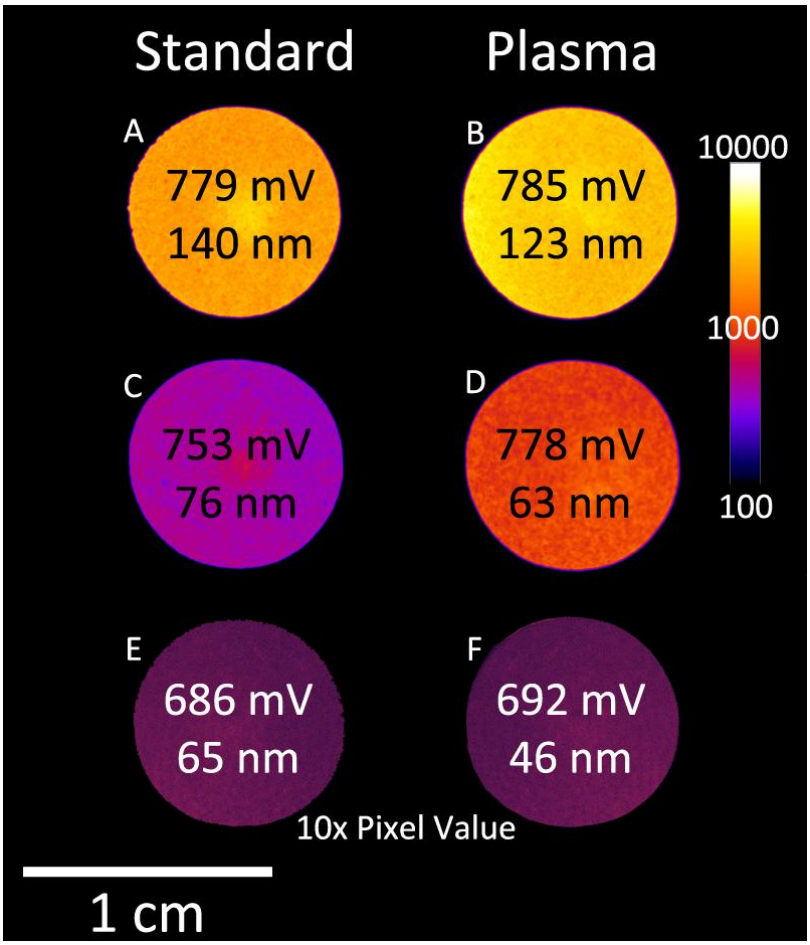

Figure 37 EL of plasma and standard cleaned TCO cells at varying CdS thicknesses.

Light-beam-induced-current (LBIC) results also demonstrate an improvement in uniformity of plasma-cleaned cells. Figure 38 compares the two thinnest CdS samples from Table 2 at short circuit and with a forward voltage bias approaching V_{mp}. At zero voltage bias, both cells are relatively uniform over the whole area, with a few extra localized defects on the standard cleaned sample. At forward bias, however, the non-uniformity is enhanced, accentuating the weak diodes. The plasma cleaned samples show better uniformity than the standard cleaned sample, both in the map and more clearly in the histogram.

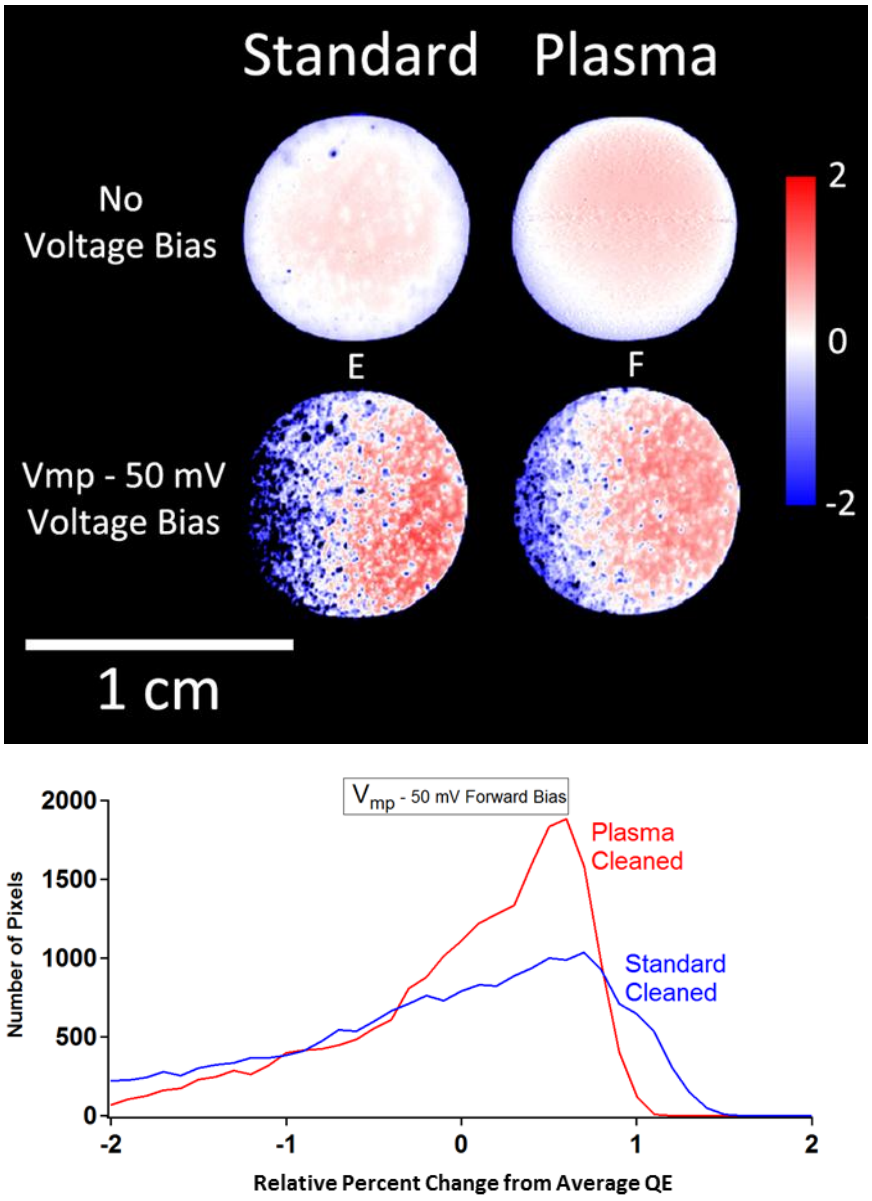

Figure 38 LBIC spatial maps of standard and plasma cleaned cells with and without forward voltage bias (top). The histogram demonstrates the spatial uniformity at bias (bottom).

Plasma cleaning of the TCO-coated glass prior to the deposition of CdS/CdTe solar cell led to improved photovoltaic efficiency of as much as 1½% absolute through increases in both current and voltage. The current increases resulted from thinner CdS following the plasma cleaning, and the improved voltage from pinhole reduction. The voltage increases were

constant with temperature and consistent with the average electroluminescence intensity. Improvement in cell uniformity from plasma cleaning was demonstrated with maps from scanning-white-light-interferometry, light-beam-induced current in forward bias, and EL intensity.

3.4 Scaling of Plasma Cleaning

With investment from Abound Solar, the project was scaled from the 3.6” x 3.1” substrate plasma cleaner, utilized by CSU’s manufacturing lab (Figure 39A), to a 10” x 10” plasma cleaning source. The scaled plasma cleaner was designed to plasma clean the center 10” x 10” area of the 16” x 16” cells produced at Abound Solar’s R&D facility (Figure 39B). The 10” x 10” prototype plasma cleaner utilized both wire and plate anode configurations and maintained similar plasma characteristic properties [54]. The 10” x 10” cleaner netted similar results to the 3.6” x 3.1” source, allowing reduced CdS thickness at no V_{oc} loss. With the successful scaling to the R&D line a collaboration was formed to scale the plasma cleaner design to a 2’ x 4’ prototype (Figure 39C). The 2’ x 4’ plasma cleaner was built and tested at CSU and then used for in-line plasma cleaning at the Abound manufacturing plant. The 2’ x 4’ cleaner allowed for similar results to CSU’s 3.6” x 3.1” source and Abound Solar’s R&D 10” x 10” sources. Figure 39 illustrates the design process from concept to implementation and to production on all three scales. Note the formation of plasma beads on the anodes of the 2’ X 4’ source were removed with improved anode material quality.

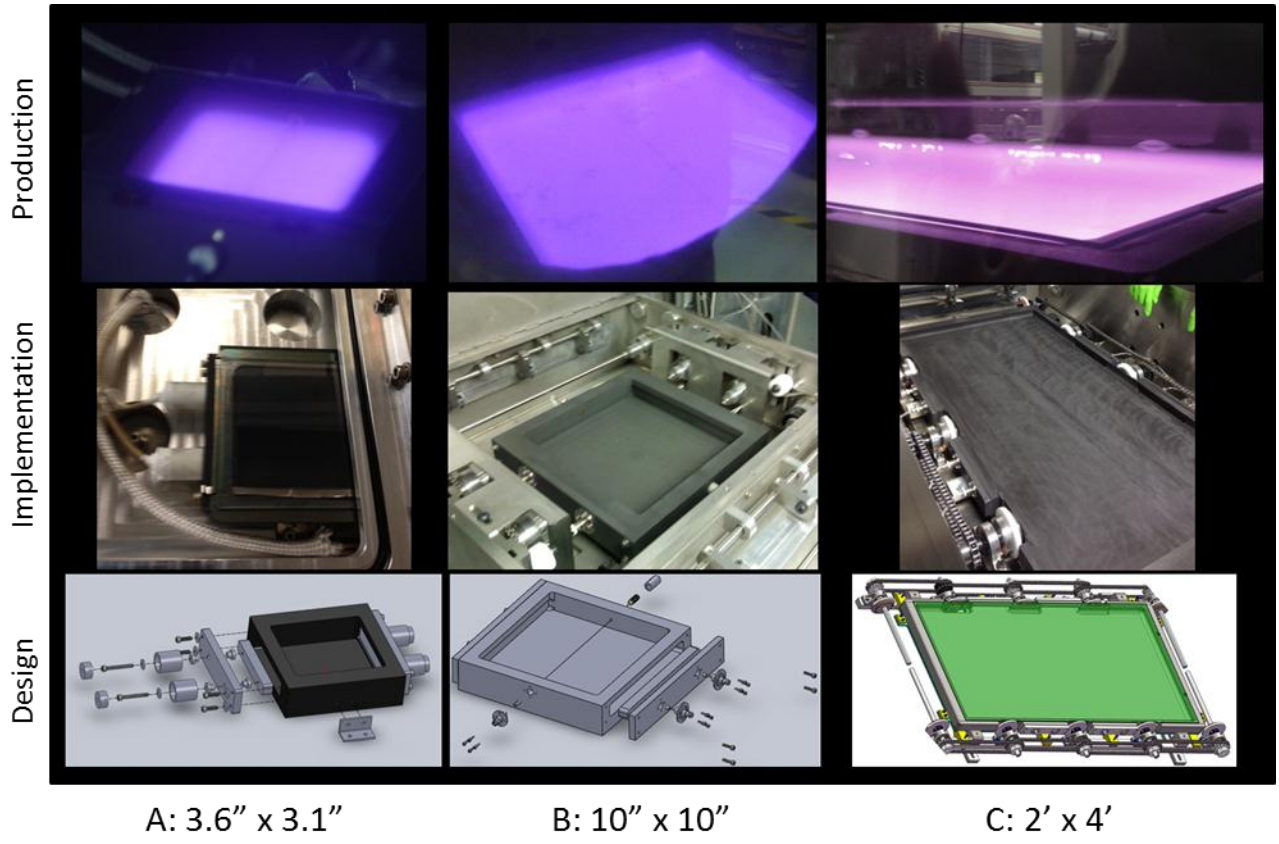

Figure 39 Development progression of plasma cleaner technology from research, prototype, to full scale production A: (3.6” x 3.1”), B: (10” x 10”), C: (2’ x 4’).

Chapter IV Plasma Enhanced Close Space Sublimation

4.1 Introduction to Plasma Enhanced Close Space Sublimation

With the recent successful scaling of the plasma cleaner and with the proven scalability of inline close space sublimation (CSS), the next research thrust was to incorporate plasma enhanced techniques into other stages of the in-line CdTe manufacturing process. To do this a hollow cathode plasma cleaner-like discharge was incorporated within a CSS source to allow the sublimating material and the film growth surface to be modified during deposition. This process is referred to as plasma enhanced close space sublimation (PECSS). It was first utilized in this thesis to widen the band gap of the window layer material (CdS) while simultaneously maintaining the rapid deposition rates of the original, non-plasma-assisted CSS process. A wider band gap window layer could be made thicker and would simplify cell fabrication by eliminating the necessity to control CdS thickness to values slightly above the voltage cliff (Figure 32). In previous work by Wu et al. and Kephart et al., high efficiency devices were generated by the addition of oxygen to the CdS [19, 57]. The following sections discuss how PECSS was used to incorporate oxygen in CdS. Full devices were fabricated with these films and performance data were compared to standard devices.

4.2 Apparatus and Procedure

Figure 40 shows the cross sectional geometry of a plasma source integrated into a CSS deposition source used at CSU [29, 30]. The PECSS design uses an increased pocket depth compared to the standard CSU pocket, and a mesh is added above the wire anode to better control plasma parameters. Similar to plasma cleaning, the wire anode is biased positive of the

grounded cathode surface to ignite and maintain the primary plasma discharge. The stainless steel or graphite mesh contains the primary plasma and keeps it from directly interacting with the substrate. The plasma present between the mesh and the substrate is referred to as the drift plasma (Figure 40). There are two primary effects to material deposition by integrating the plasma into the CSS deposition source. First, the primary plasma breaks up the injected gas into various atomic and ionized states, allowing different compounds to form from the sublimating material and plasma products. Second, the ions from the drift plasma bombard the substrate and ion assist the growth of the film, which can be used to control grain size and structure.

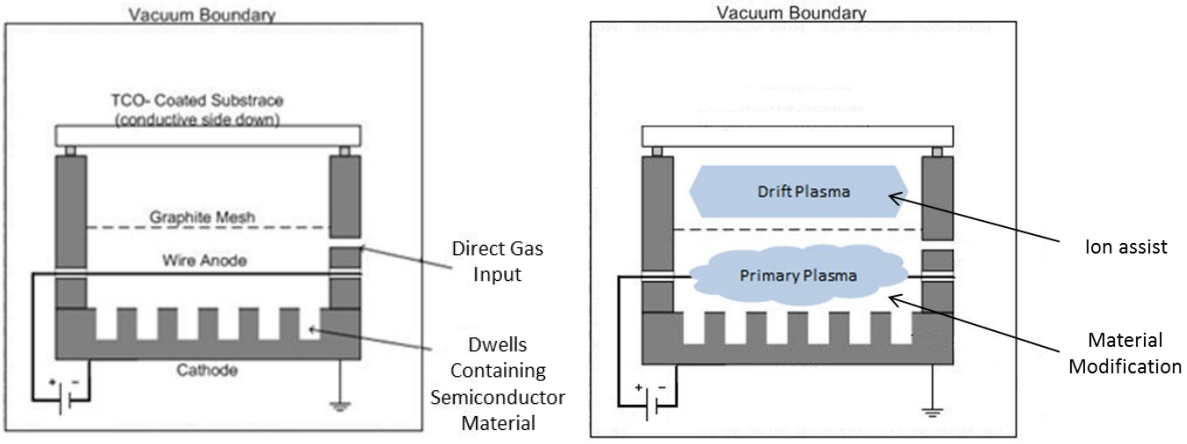

Figure 40 Sketch of plasma enhanced close space sublimation (PECSS) showing A: Geometry B: Plasmas regions.

The PECSS source was installed in an in-line deposition system and used to produce CdS/CdTe devices. The PECSS hardware uses a tungsten 0.25mm wire as the anode and a woven 50% open stainless steel or 33% open graphite mesh to contain the primary plasma. The plasma is ignited and sustained by a Glassman High Voltage 300 W power supply. To improve uniformity the plasma discharge was pulsed using a function generator connected to the power

supply. A controlled ratio of N_2 and O_2 gas was directly injected into the pocket. The plasma discharge and deposition were performed at 40 mTorr, which was defined by CSS process conditions currently used at CSU in the inline cell fabrication tool. The following parameters were fixed unless otherwise stated. The plasma was pulsed at 20 Hz, gas was injected at 1 sccm, gas composition was 80% N_2, 20% O_2, and the average plasma power was ~25 watts.

4.3 Results of CdS:O films and devices created using PECSS

Figure 41A depicts a SEM image of a CdS film deposited using the standard (non-plasma assisted) close space sublimation source. The film exhibits a crystalline structure with grains on the order of 100-300 nm in size. Figure 41B shows an image of a CdS:O film deposited with PECSS, the film indicates a strong reduction in grain size down to 20nm. This reduction in grain size agrees with results from CdS:O films generated using RF sputtering [19]. To determine whether the CdS was incorporating oxygen into the film; UV-Vis, XPS, and EDS analysis were performed.

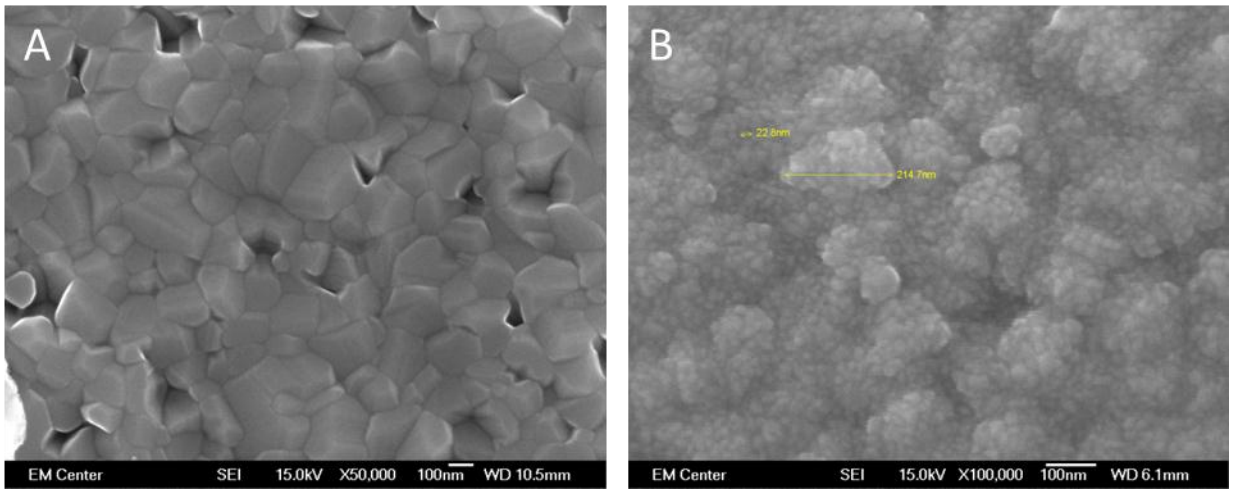

Figure 41 SEM planer Images A: CSS CdS (50,000x), B: PECSS CdS:O (100,000x).

Figure 42 compares UV-Vis measurements of CdS and CdS:O films that were 170 nm in thickness. It is important to note that any drop in transmission within the AM 1.5 solar sun spectrum translates to a reduction in device current and ultimately performance. The CdS film data show a band gap at ~500 nm (2.4 eV), and as discussed in Chapter 3, this can reduce short circuit current by 4.6 mA/cm^2. However, by using PECSS, the band gap of the film was widened, reducing CdS absorption and suggesting that oxygen was incorporated into the CdS.

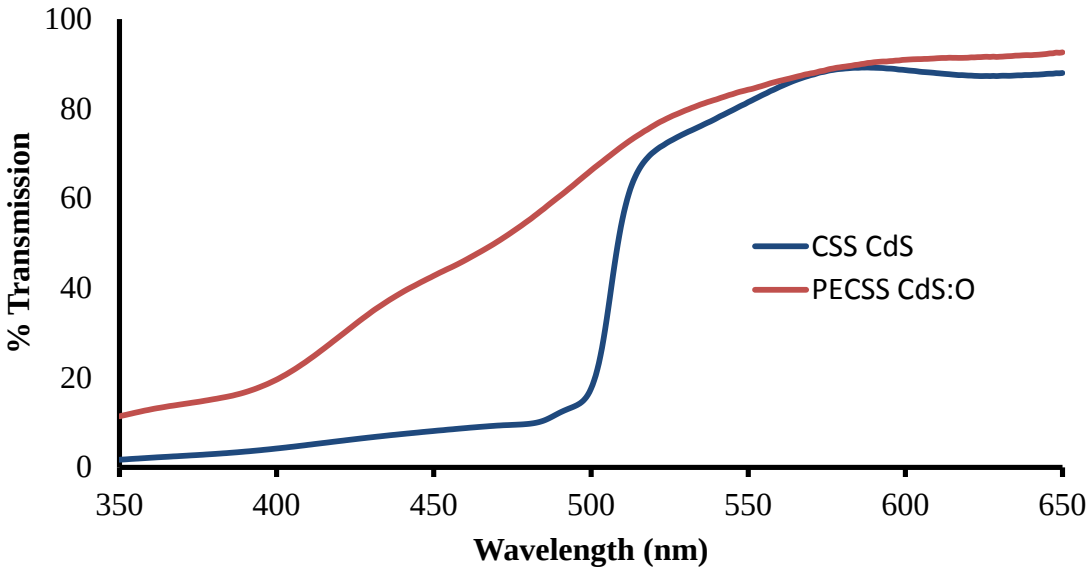

Figure 42 UV-Vis Measurement of CdS and CdS:O of films that were 170 nm in thickness.

Figure 43 shows an XPS wide spectrum sweep of the CdS:O film that was acquired to quickly assess material composition. The wide spectrum sweep reveals an oxygen peak along with cadmium, sulfur, and carbon. Concentrations of these constituents are displayed in the legend, but are considered to be approximate as the resolution is low in a wide spectrum sweep. To increase resolution the sweep rate was reduced and centered on the elements; cadmium, sulfur, oxygen, and carbon that were uncovered in the preliminary spectrum.

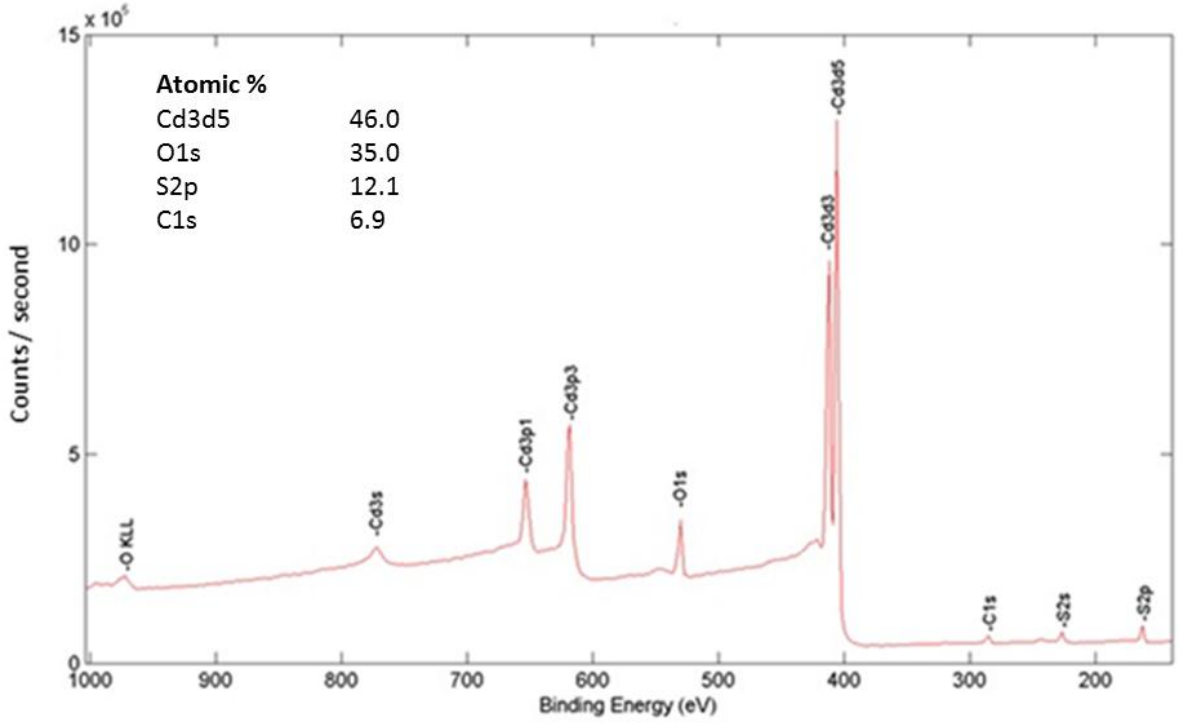

Figure 43 XPS Spectrum Sweep of CdS:O PECSS Sample at 50% N_2 – 50% O_2 injection ratio.

Table 3 summarizes concentrations of the four elements of interest and was performed for three different gas injection ratios. It is noted that the film was exposed to atmosphere before performing XPS measurements allowing absorption of atmosphere gases onto the surface of the film. Consequently, argon sputtering was used to remove the surface absorbed contaminates. Specifically, the film received a 2 kV, 180 second Argon sputter treatment. It is noted that these films all have the same ~120 nm CdS and CdS:O film thickness and the ion etch removes ~¼ of the CdS or CdS:O film.

Table 3 Concentration of key elements vs. injection gas ratio measured with XPS.

	Gas Injection Ratio			
	No Injection No Plasma	80% N_2 - 20% O_2 PECSS	50% N_2 - 50% O_2 PECSS	Atomic %
Cadmium (Cd)	55%	55%	55%	
Sulfur (S)	44.9%	34%	12.5%	
Oxygen (O)	0.0%	10%	32%	
Carbon (C)	0.1%	0.5%	0.5%	

Figure 44 displays XPS oxygen peaks for the CdS and CdS:O films at the three different gas injection ratios. The CSS deposited CdS film shows no oxygen incorporation, but upon direct injection of a low concentration of oxygen (20% O_2) into the plasma enhanced source, oxygen was incorporated into the film at moderate atomic concentrations. As the gas injection ratio was increased to a higher concentration (~50% O_2), the oxygen incorporation into the film increases to 30%. This suggests that the amount of oxygen incorporated into the CdS film was controlled by the concentration of oxygen being flown into the pocket when plasma conditions were fixed.

The two separate peaks in Figure 44 represent the oxygen sitting at two different energy states within the material. Using the National Institute of Standards and Technology (NIST) XPS database the peak on the left was identified as cadmium sulfate ($CdSO_4$) while the peak on the right was cadmium oxide (CdO) [58]. As the oxygen injection ratio was increased the CdO peak increases, with the $CdSO_4$ peak remaining constant. From inspection of Table 3, one can

conclude that the atomic percent of cadmium remains constant for all of the films. As the oxygen peak increases however, the sulfur peak decreases, which implies that oxygen was replacing sulfur.

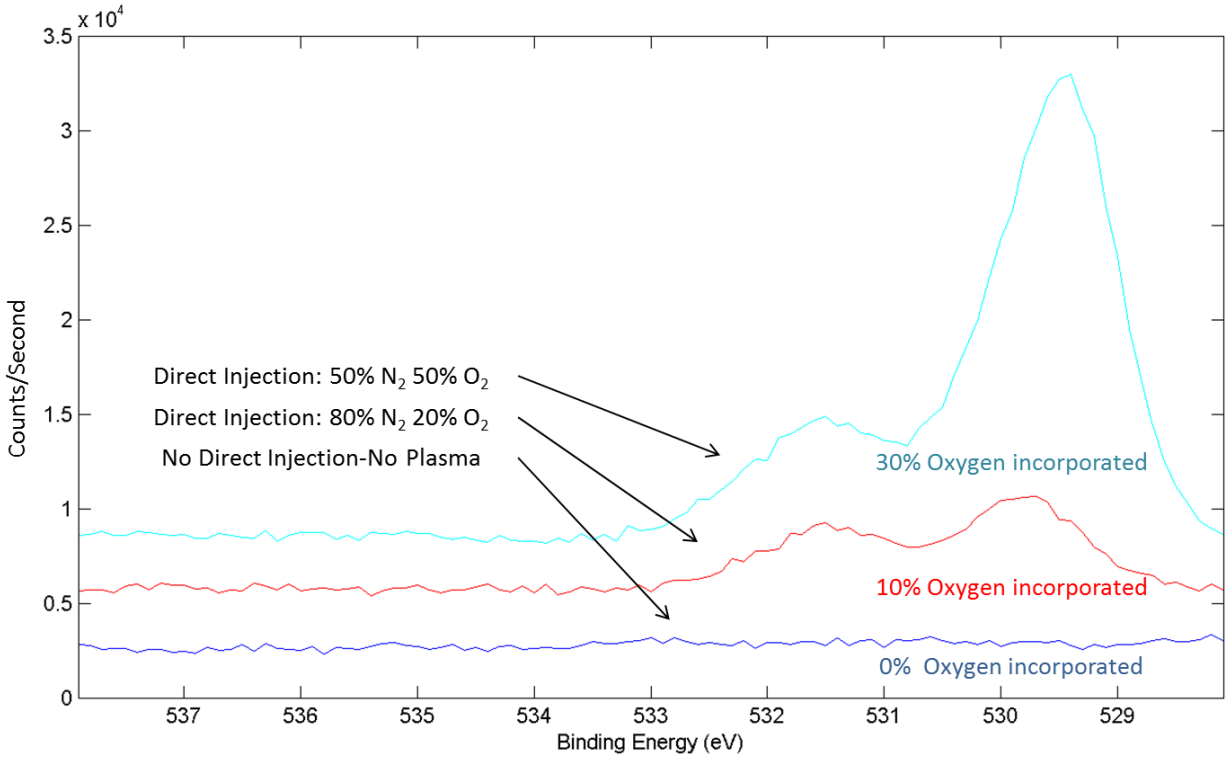

Figure 44 XPS sweep of oxygen peak with high and low oxygen concentration.

Since the films received a sputter treatment at energies high enough to break bonds and preferentially sputter material before collecting XPS data, it is important to note that film composition can be altered. Sample transportation in clean inert environments and lower energy cleaning techniques might improve XPS concentration accuracy [59].

Figure 45 compares EDS data of a CSS CdS film to a PECSS CdS:O film. EDS was performed at 15kV and results in a tear drop penetration of the EDS electron beam into the

film. This results in an X-ray response from both the CdS layer and the underlining TCO layer, and it is concluded that the small oxygen peak present in the CSS film is most likely from the TCO. Figure 45B shows a significant increase in oxygen concentration from the sample receiving the plasma enhanced treatment along with a compensating decrease in sulfur. With both films being the same thickness, the EDS data imply that the plasma enhanced sample has incorporated oxygen, supporting the XPS data above.

A: CSS CdS

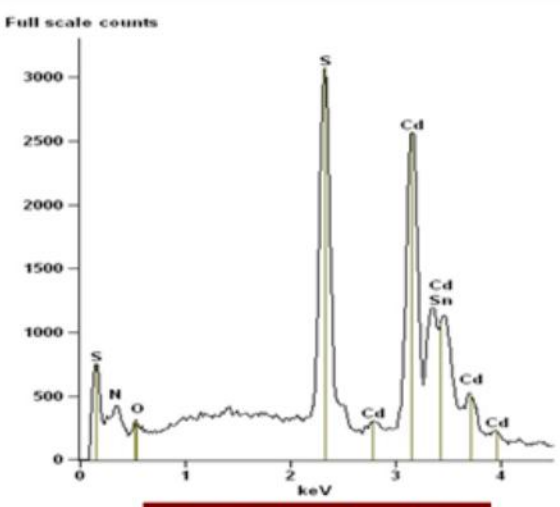

Element Line	Weight %	Atom %
N K	0.00	0.00
O K	0.00	0.00
S K	15.05	38.66
Cd L	61.55	45.10
Sn L	23.40	16.24
Total	100.00	100.00

B: PECCS CdS:O

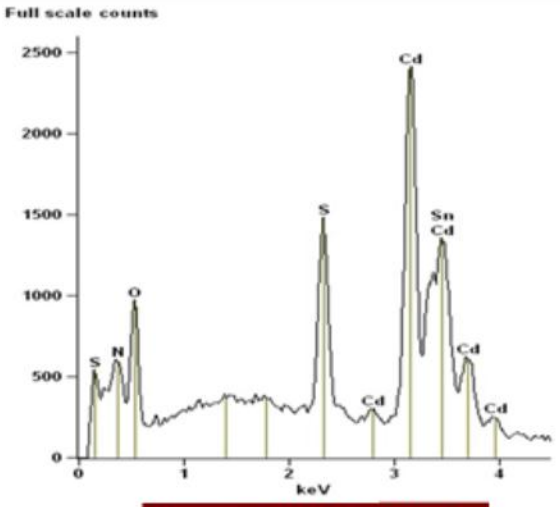

Element Line	Weight %	Atom %
N K	3.14	13.51
O K	8.58	32.29
S K	5.63	10.57
Cd L	52.58	28.17
Sn L	29.96	15.20
Total	100.00	100.00

Figure 45 EDS of A: CSS CdS and B: PECSS CdS:O.

The CdS and CdS:O films were then processed through the CdTe in-line deposition system to form CdS/CdTe and CdS:O/CdTe devices. Figure 46 shows an improved blue photon QE response of the PECSS CdS:O/CdTe device in comparison to the CdS/CdTe device. Similar to

results shown in UV-Vis data in Figure 42, the incorporation of oxygen has resulted in a reduction of blue photons being absorbed with in the window layer. This results in an increased current from the cell, a cell response that is similar to thinning the CdS without the danger of reducing the cell voltage.

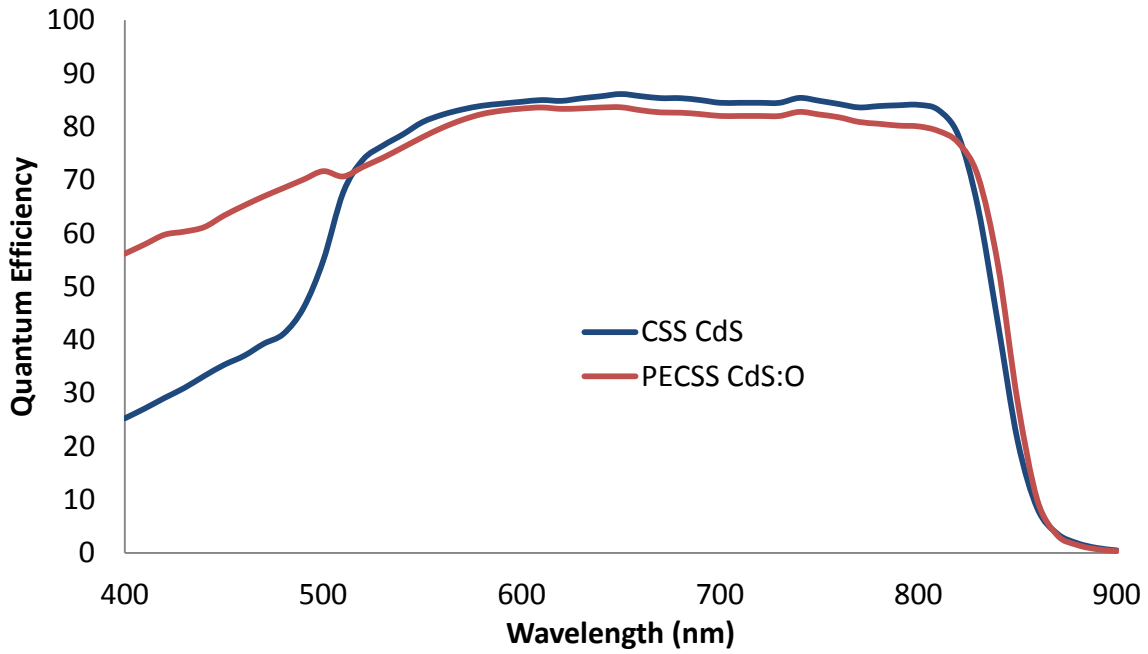

Figure 46 QE of CdS and CdS:O samples.

Figure 47 demonstrates the J-V curves for the CdS and CdS:O devices. The voltages of the two cells are similar, resulting in an improved efficiency from the CdS:O device. With similar fill factors, open circuit voltage, and improved current density; the PECSS source mimics improvements shown in creating CdS:O films with RF sputtering techniques. The PECSS process incorporated oxygen into the film to concentrations similar to Wu el al. [19, 57] and increased cell efficiency by 1.2%.

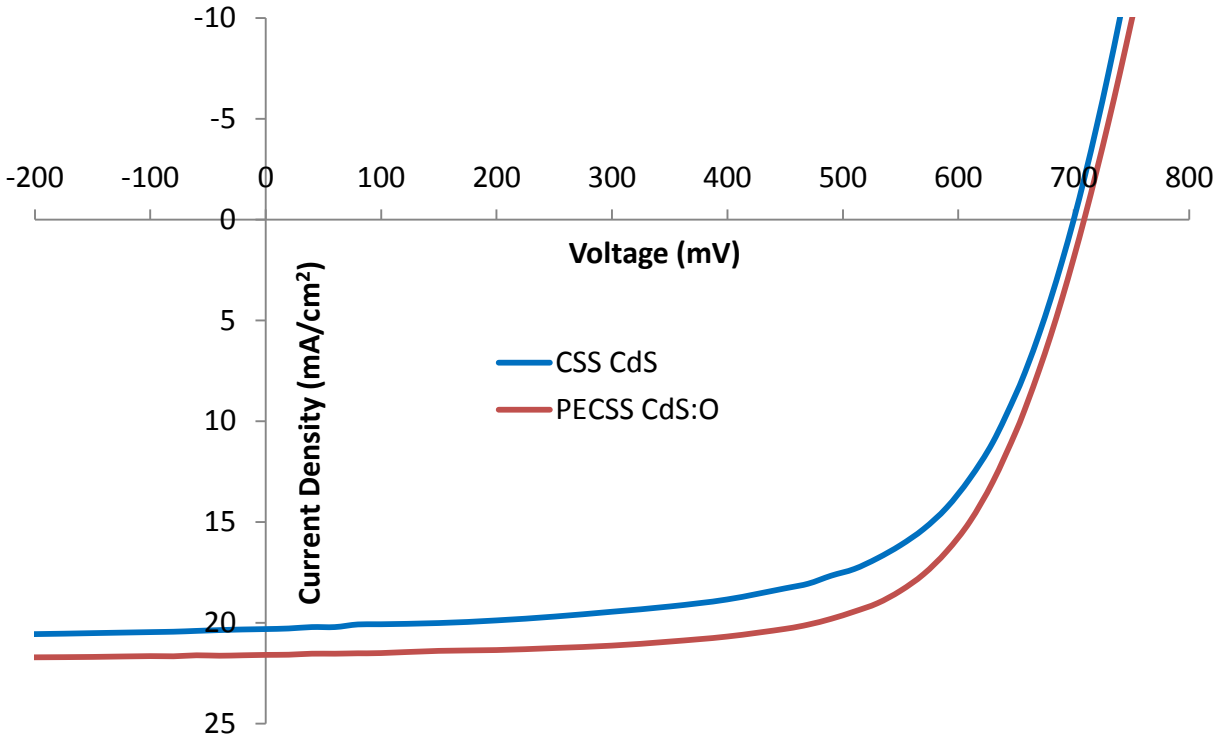

Figure 47 J-V of CdS and CdS:O films.

Chapter V Conclusion and Future Work

There is a growing environmental and economic need for alternative energy production. Solar energy provides a clean and abundant solution for this need. With many potential solar cell technologies, CdTe thin film photovoltaic cells demonstrate a near optimal Shockley-Quasar band gap and proven scalable methods exist for manufacturing. What is needed to make the CdTe cell more economically viable is to further reduce cell production cost while simultaneously improving cell efficiencies. This thesis presented two solutions for improving the CdTe solar cell efficiency. First, the development of an inline plasma cleaning treatment of the transparent conductive oxide (TCO) was described for improving surface cleanliness prior to film deposition. Second, the sublimation deposition processes used at CSU was enhanced by incorporating the plasma cleaning discharge into the CSS source. This plasma enhanced close space sublimation (PECSS) process was used to incorporate oxygen into the CdS window layer to increase its transparency. Both plasma cleaning and PECSS processes have been used to fabricate CdS/CdTe solar cells and have demonstrated cell efficiency improvements.

5.1 Plasma Cleaning

Plasma cleaning of the TCO-coated glass prior to the deposition of the CdS/CdTe solar cell strongly affects to the TCO surface, the subsequently deposited CdS film, and CdS/CdTe devices. First, the plasma cleaned TCO film exhibits increased hydrophilic behavior, which indicates a reduction or elimination of surface contaminates. When CdS films are deposited onto a plasma cleaned TCO surface poor growth regions (pin holes) are eliminated compared to CdS films deposited on substrates that use industry standard cleaning techniques. Cells

manufactured on plasma cleaned TCO resulted in improved photovoltaic efficiency by as much as 1.5%. The cell current was increased from (1) the ability to thin CdS by ~20nm at no Voc loss and (2) by improved voltage at all CdS thicknesses from eliminating pinholes. The voltage increases observed on plasma cleaned devices were constant with temperature and consistent with the electroluminescence intensity. The cell uniformity was improved by plasma cleaning as demonstrated with maps collected using scanning-white-light-interferometry, light-beam-induced current in forward bias, and electroluminescence.

The plasma cleaning process was scaled from the CSU 3.6” X 3.1” research device to a 10” x 10” R&D device, and then to a full production scale at 2’x4’. The sources were developed, built, and tested at CSU and devices fabricated with both the R&D and production scale plasma cleaners demonstrated similar efficiency improvements as shown in Chapter III.

5.2 Plasma Enhanced Close Space Sublimation

With the recent successful scaling of the plasma cleaner and with the proven scalability of inline close space sublimation (CSS), the next research thrust was to incorporate plasma enhanced techniques into other stages of the in-line CdTe manufacturing process. To do this a hollow cathode plasma cleaner discharge was incorporated within a CSS source to allow the sublimating material and the film growth surface to be modified during deposition. This process was termed plasma enhanced close space sublimation (PECSS). It was utilized in this thesis to widen the band gap of the window layer material (CdS) while simultaneously maintaining the rapid deposition rates of the original, non-plasma-assisted CSS process. By using the plasma enhanced CdS source oxygen was incorporated into CdS, widening the band gap and resulting

in improved device current at no voltage loss. Oxygen incorporation in CdS was presented with XPS and EDS data, showing a relationship between the injection gas composition and the percent of oxygen incorporated into the CdS film (CdS:O). The wide band gap of CdS:O reduced the absorption of high energy blue photons as demonstrated with UV-Vis measurements of CdS:O films and QE measurements on completed devices. The CdS:O/CdTe devices demonstrated increased cell current (Jsc) at a constant cell voltage response resulting in an efficiency improvement of 1.2% compared to control CdS/CdTe devices.

5.3 Plasma Cleaning Future Work

The plasma cleaning treatment has utilized the same process gas since preliminary set points were established. As plasma power and time were investigated, the gas composition was maintained at 98% N_2 - 2% O_2 concentration, which is the gas composition used within the in-line CdTe manufacturing process at CSU. This background gas will affect plasma properties and the resulting surface conditions [23, 60]. To further reduce CdS thickness requirements and increase voltage, different oxygen concentrations in the background gas should be investigated.

To limit inducing unintentional variability the post treatment conditions of the devices grown on plasma cleaned and standard cleaned TCO substrates were held constant over varying CdS thicknesses. To enhance the plasma cleaning effect, the post-treatment conditions should be varied to establish new set points for the thinner, pin-hole free CdS, from plasma cleaned TCO. The post-treatments include the passivation of CdTe with $CdCl_2$ and doping of the back of CdTe with $CuCl_2$ treatment [29].

5.4 Plasma Enhanced Close Space Sublimation CdS:O Future Work

Figure 48 shows UV-Vis data of CSS CdS and PECSS CdS:O films and the QE response of those exact same films after being made into devices. The difference in UV-Vis data of the CSS CdS and PECSS CdS:O is 10%. After those films are processed to full devices the blue photon QE response displays a 40% increase. This drastic increase in QE response should be investigation further to uncover why this is occurring.

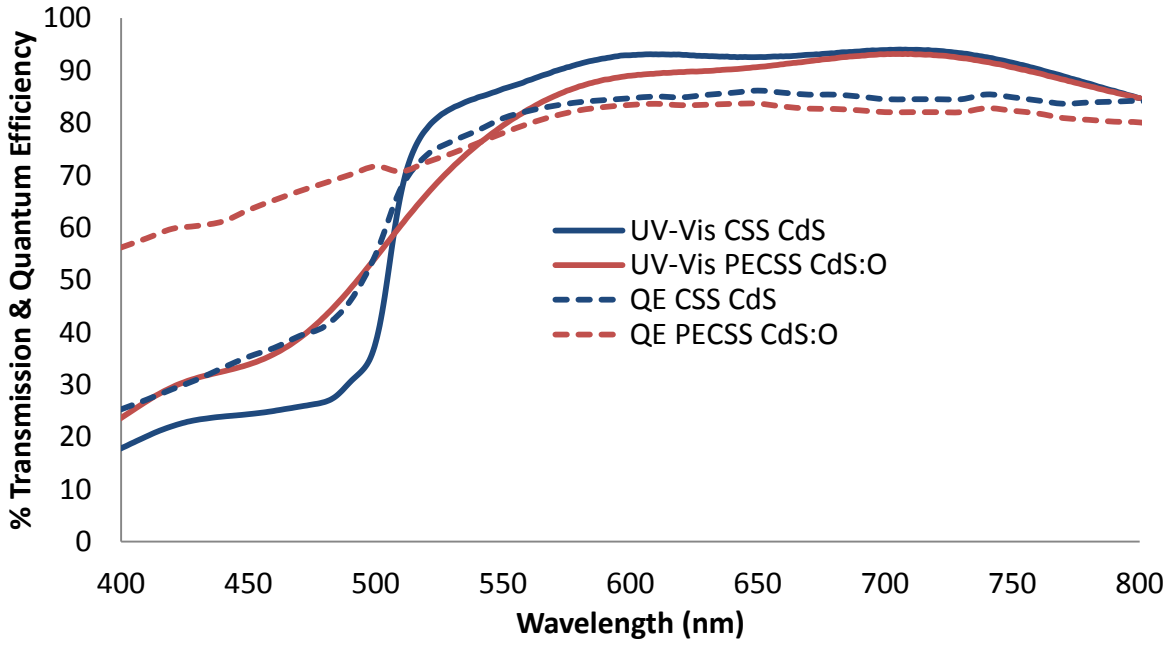

Figure 48 UV-Vis and QE of CdS and CdS:O.

5.5 Plasma Enhanced Close Space Sublimation Future Work

The recent record cells generated for CdTe have focused on improving the short circuit current parameter of the cell [19, 61]. Using methods such as thinning CdS, CdS:O and addressing glass losses such as reflection, glass absorption, and TCO absorption. First Solar's record cell revealed a short circuit current of 27.23 mA/cm^2, obtaining ~90 % of available

current. The dominant problem that remains is the excessive voltage losses that are observed in CdTe cells (21). The First Solar's record cell, and all record cells before it, have an open circuit voltages around 0.850 V, which represents only ~75% of the available voltage.

To further improve CdTe cells, innovative ideas are needed to improve the open circuit voltage. Potential solutions to this issue include the formation of an electron reflector, use of single crystal CdTe, or increased doping of the CdTe film. Currently the fabrication of an electron reflector is being developed at CSU. An Electron reflector uses the formation of a high band gap material placed within the depletion region of the cell near the back contact to allow the formation of a conduction band barrier [30]. Single crystalline CdTe would essentially remove any grain boundaries from within the depletion width and would reduce recombination and defects, but this requires CdTe fabrication technologies with unproven scale-ability. With the development of PECSS the increased in situ doping of polycrystalline CdTe is possible while maintaining the rapid deposition rates of CSS. As shown in Chapter 4, gas injection composition and plasma parameters could be adjusted to modify the semiconductor film.

Currently the sublimated CdTe has a carrier concentration ~10^{14} cm^{-3}, with CdTe absorbing 99% of light at 1 um thickness, a carrier concentration around 10^{16} cm^{-3} would allow for better matching of the depletion width to 1 um and for an increase in voltage. With the plasma enhanced close spacing sublimation source, CdTe would be sublimated through plasmas containing known dopants, such as nitrogen and arsenic for example to dope the film and increase free carrier concentration.

5.6 Plasma Enhanced Close Space Sublimation CdTe:N Future Work

For preliminary results of increased CdTe doping, nitrogen was introduced into the plasma enhanced environment during CdTe deposition (CdTe:N). The PECSS CdTe:N results in a decreased grain size compared to untreated CdTe films. The cell, prior to $CdCl_2$ treatment, exhibits an enhanced open circuit voltage increase of 10% over standard pre-$CdCl_2$ treated cells. After $CdCl_2$ treatment the CdTe:N films exhibit a visual difference densification of grains (Figure 49 A&B). As shown in Figure 49D, there is a decrease in grain size along with reduced open area between grains. The CdTe:N film results in a 9% increase in open circuit voltage of the cell compared to the control CdTe sample. However, the CdTe:N cell voltages are still within the standard record cell voltages generated in the CSU inline CdTe manufacturing tool. In future work further investigation of plasma parameters and gas composition to improve cell voltages should be investigated.

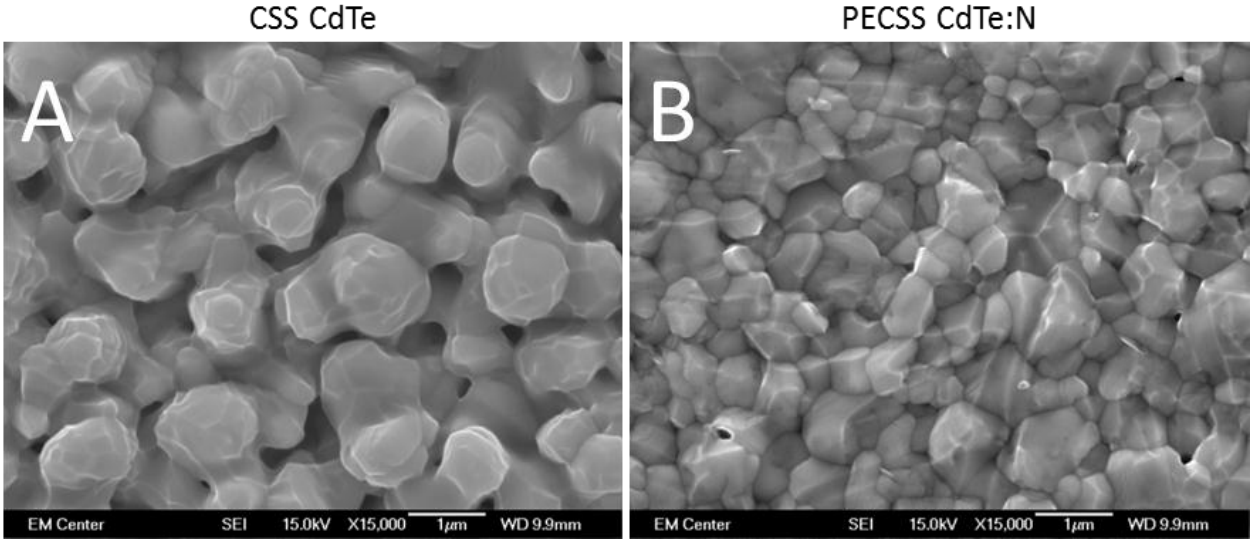

Figure 49 SEM Image of CdTe sample with $CdCl_2$ post-treatment A: CSS CdTe, B: PECSS CdTe:N.

References

[1] "Global Energy Statistical Yearbook 2012." *World Energy Statistics*. Enerdata. Web. 02 Oct. 2012. <http://yearbook.enerdata.net/>.

[2] United Nations, Department of Economics and Social Affairs, Population Division (2011): World Population Prospects, the 2010 Revision. New York

[3] Lynn Orr, *Changing the world's energy systems*, Stanford University Global Climates & Energy Project, 2006.

[4] CNRS (Délégation Paris Michel-Ange). "Predicted increase in atmospheric CO2 will directly affect living organisms: Carbon dioxide exacerbates oxygen toxicity." *ScienceDaily*, 4 Mar. 2011. Web. 26 Sep. 2012.

[5] Hertzberg, Martin. "CO2 Is Not the Problem." *Breckenridge & Summit County Colorado*. Summit Daily, 27 Feb. 2012. Web. 26 Sept. 2012. <http://www.summitdaily.com/article/20120227/LETTER/120229874>.

[6] Hoffman, Doug L. "The Resilient Earth." *Reply to Comment*. The Resilient Earth, 2008. Web. 25 Sept. 2012. <http://theresilientearth.com/?q=comment/reply/424>.

[7] Dr. Pieter Tans, NOAA/ESRL (www.esrl.noaa.gov/gmd/ccgg/trends/) and Dr. Ralph Keeling, Scripps Institution of Oceanography (scrippsco2.ucsd.edu/)

[8] U.S. Department of Energy, *2009 Renewable Energy Data Book*, Energy Efficiency & Renewable Energy, August 2010. pp. 3,4,(was 17)

[9] Shahan, Zachary. "70% of New EU Power from Renewable Energy in 2011 (47% Solar, 21% Wind)." *Clean Technica*, 7 Feb. 2012. Web. 25 Sept. 2012. <http://cleantechnica.com/2012/02/07/70-of-new-eu-power-from-renewable-energy-in-2011-47-from-solar-21-from-wind/>.

[10] Weston A. Hermann, Quantifying Global Energy Resources, Elsevier, Vol 31 pp. 1685-1702, 2006.

[11] "About SunShot." *SunShot Initiative*. U.S. Department of Energy, 16 Nov. 2011. Web. 25 Sept. 2012. <http://www1.eere.energy.gov/solar/sunshot/about.html>.

[12] William Shockley and Hans J. Queisser, "Detailed Balance Limit of Efficiency of p-n Junction Solar Cells", *Journal of Applied Physics*, Volume 32 (March 1961), pp. 510-519, with added current cell efficiencies as of 2012.

[13] "Band Theory of Solids." *Band Theory for Solids*. Department Of Physics, George State University, Jan. 2005. Web. 25 Sept. 2012. <http://hyperphysics.phy-astr.gsu.edu/hbase/solids/band.html>.

[14] Tilley, R. J. D. *Understanding Solids: The Science of Materials*. Chichester, West Sussex: John Wiley & Sons, 2004. Print.

[15] Rako, Paul. "Integration in the Other Direction." *EDN Europe*. N.p., Mar. 2010. Web. 25 Sept. 2012. Web. http://www.edn-europe.com/integrationintheotherdirection +article +3854+ Europe. html.

[16] Jeffery L. Gray, Physics of a Solar Cell, Purdue University, West Lafayette, Indiana, USA, 2003 pp. 63, 84-85

[17] "Solar Spectral Irradiance: Air Mass 1.5." *Solar Spectral Irradiance: Air Mass 1.5*. NREL, Web. 25 Sept. 2012. <http://rredc.nrel.gov/solar/spectra/am1.5/>.

[18] United States Committee on Extension to the Standard Atmosphere, "U.S. Standard Atmosphere, 1976", National Oceanic and Atmospheric Administration, National Aeronautics and Space Administration, United States Air Force, Washington D.C., 1976.

[19] X. Wu, High-efficiency polycrystalline CdTe thin-film solar cells, Elsevier, 77 pp.803-814, 2004

[20] Streetman, Ben G., and Sanjay Banerjee. *Solid State Electronic Devices*. Upper Saddle River, NJ: Prentice Hall, 2000. Print.

[21] Madelung, Otfried. *Semiconductors - Basic Data*. Berlin, u.a.: Springer, 1996. Print

[22] Irvine, S., V. Barrioz, D. Lamb, E. Jones, and R. Rowlandsjones. "MOCVD of Thin Film Photovoltaic Solar Cells—Next-generation Production Technology?" *Journal of Crystal Growth* 310.23 (2008): 5198-203. Print.

[23] Fritsche, J., S. Gunst, A. Thiben, R. Gegenwart, A. Klein, and W. Jaegermann. "CdTe Thin Film Solar Cells: The CdS/SnO2 Front Contact." *Materials Research Society* 668 (2001): n. pag. Print.

[24] Alan R. Davies, Effects of Contact-Based Non-Uniformities in CdS/CdTe Thin Film Solar Cells, Dissertation, Colorado State University, Department of Physics, 2008

[25] Tashkandi, M. A. , Sampath W. S., Eliminating Pinholes in CSS Deposited CdS Films, 38th PVSC IEEE Conference, 2012.

[26] Swanson D.E., Lutze R.M., Sampath W.S., Williams J.D., Plasma Cleaning of TCO Surfaces Prior to CdS/CdTe Deposition, 38th PVSC IEEE Conference, 2012

[27] Galymzhan T. Koishiyev, James R. Sites, Effect of Shunts on Thin-Film CdTe Module Performance, Materials Research Society, 2009

[28] S.H. Demtsu, J.R. Sites, Quantification of Losses in Thin-Film CdS/CdTe Solar Cells, 31st IEEE PVSC conference, pp. 347-350, 2005

[29] K.L. Barth, R. A. Enzenroth, W. S. Sampath, US Patent No. 6, 423, 565, 23 July 2002

[30] P. Kobyakov, J. Kephart, and W. Sampath, "Sublimation of Mg onto CdS/CdTe films fabricated by advanced deposition system," in 37th IEEE Photovoltaic Specialists Conference PVSC, 2011

[31] K. Von Rottkay, M. Rubin, Optical Indices of Pyrolytic Tin-Oxide Glass, LBNL Publication 38586, 1996.

[32] Vo, Kevin. "Spectrophotometer." *UC Davis Chemestry*. ChemWiki, 19 June 2011. Web. 27 Sept. 2012. <http://chemwiki.ucdavis.edu/Physical_Chemistry/Kinetics/Reaction_Rates/Experimental_Determination_of_Kinetcs/Spectrophotometry>.

[33] Deck, Leslie, and Peter De Groot. "High-speed Noncontact Profiler Based on Scanning White-light Interferometry." *Applied Optics* 33.31 (1994): 7334. Print.

[34] Zisman, W. A. "Relation of the Equilibrium Contact Angle to Liquid and Solid Constitution." *U.S. Naval Research Laboratory* (1964): n. pag. Print.

[35] Yang, Jianguo. "Use of the Equilibrium Contact Angle as an Index of Contact Surface Cleanliness." Thesis. Oregon State University, 1990. Print.

[36] Rame-hart. "Information on Contact Angle." *RamÃ©-hart Contact Angle*. N.p., n.d. Web. 27 Sept. 2012. <http://www.ramehart.com/contactangle.htm>.

[37] Woods, Susan. "Understanding Scanning White Light Interferometry." *Micro Manufacturing* 2.4 (2009): n. pag. Print.

[38] Binnig, G., and C. F. Quate. "Atomic Force Microscope." *Physical Review Letters* 56.9 (1986): 930-33. Print.

[39] "Atomic Force Microscopy." *Wikipedia*. Wikimedia Foundation, 18 Sept. 2012. Web. 27 Sept. 2012. <http://en.wikipedia.org/wiki/Atomic_force_microscopy>.

[40] Turner, Noel H. "Surface Analysis: X-ray Photoelectron Spectroscopy and Auger Electron Spectroscopy." *Analytical Chemistry* 58.5 (1986): 153-65. Print.

[41] Hollander, Jack M., and William L. Jolly. "X-ray Photoelectron Spectroscopy." *Accounts of Chemical Research* 3.6 (1970): 193-200. Print.

[42] "X-ray Photoelectron Spectroscopy." *Wikipedia*. Wikimedia Foundation, 21 Sept. 2012. Web. 27 Sept. 2012. <http://en.wikipedia.org/wiki/X-ray_photoelectron_spectroscopy>.

[43] Laurin, Mathias. "Principle of X-ray Photoelectron SpectroscopyÂ (XPS)." *Principle of X-ray Photoelectron Spectroscopy (XPS)*. Texample, 26 Aug. 2009. Web. 27 Sept. 2012. <http://www.texample.net/tikz/examples/principle-of-x-ray-photoelectron-spectroscopy-xps/>.

[44] Konvalina, Ivo, and Ilona Müllerová. "The Trajectories of Secondary Electrons in the Scanning Electron Microscope." *Scanning* 28.5 (2006): 245-56. Print.

[45] Atteberry, Johnathan. "How Scanning Electron Microscopes Work." *HowStuffWorks*. A Discovery Company, 1998. Web. 27 Sept. 2012. <http://science.howstuffworks.com/scanning-electron-microscope2.htm>.

[46] "Energy-dispersive X-ray Spectroscopy." *Wikipedia*. Wikimedia Foundation, 18 Sept. 2012. Web. 27 Sept. 2012. <http://en.wikipedia.org/wiki/Energy-dispersive_X-ray_spectroscopy>.

[47] Nagle, Timothy J. "Quantum efficiency as a device-physics interpretation tool for thin-film solar cells." Thesis. Colorado State University, 2007. Print.

[48] John Raguse, J. Tyler McGoffin and James R. Sites, Electroluminescence System for Analysis of Defects in CdTe Cells and Modules, 38th PVSC IEEE Conference, 2012

[49] Jason F. Hiltner, Investigation of Spatial Variation in Collection Efficiency of Solar Cells, Dissertation, Colorado State University, Department of Physics, 2001

[50] K. Takechi, M. A. Lieberman. "Effect of ion energy on photoresist etched in an inductively coupled, traveled wave driven, large area plasma source." Journal of Applied Physics, Vol 89 No.10, 2001.

[51] C. P. Jean, "An overview of ion sputtering physics and practical implications," Journal of Materials Science, Vol. 18.5, 1983.

[52] U. Cvelbar, S. Pejovnik, M. Mozetie, A. Zalar, "Increased surface roughness by oxygen plasma treatment of graphite/polymer composite," Applied Surface Science, Vol. 210 No. 3, 2003.

[53] Xuekun Lu, Hui Huang, Nikolay Nemchuk, and Rodney S. Ruoff, "Patterning of highly oriented pyrolytic graphite by oxygen plasma etching," Applied Physics Letters, Vol. 75 No. 2, 1999.

[54] Metz, Garrett. "CHARACTERIZATION OF A PLASMA REACTOR DEVICE FOR PHOTOVOLTAIC APPLICATIONS." Thesis. Colorado State University, 2012. Print.

[55] R. Gueroult, P.Q. Elias, D. Packan, J. Bonnet, J.M. Rax, "Particle in cell modeling of the observed modes of a dc wire discharge," *Journal of Physics D: Applied Physics*, Volume 43, 2010.

[56] Batzill, M., and U. Diebold. "The Surface and Materials Science of Tin Oxide." *Progress in Surface Science* 79.2-4 (2005): 47-154. Print.

[57] J. Kephart, Russell Geisthardt, and W. Sampath, "Sputtered Oxygenated CdS Window Layers for Higher Current in CdS/CdTe Thin-Film Solar Cells," in 38th IEEE Photovoltaic Specialists Conference PVSC, 2012.

[58] NIST X-ray Photoelectron Spectroscopy Database, Version 3.5 (National Institute of Standards and Technology, Gaithersburg, 2003); http://srdata.nist.gov/xps/.

[59] Hanks, D., M. Weir, K. Horsely, T. Hofmann, L. Weinhardt, M. Bar, P. Kobyakov, W. Sampath, and C. Heske. "Photoemission Study of CdTe Surfaces After Low-Energy Ion Treatments." *38th IEEE PVSC Conference* (2012): Print.

[60] Batzill, M., and U. Diebold. "The Surface and Materials Science of Tin Oxide." *Progress in Surface Science* 79.2-4 (2005): 47-154. Print.

[61] First Solar. *First Solar Sets World Record for CdTe Solar PV Efficiency*. First Solar, 26 July 2011. Web. 14 Oct. 2012. <http://investor.firstsolar.com/releasedetail.cfm?releaseid=593994>.